Supplementary Information :
Creating and controlling global Greenberger-Horne-Zeilinger entanglement on quantum processors

Contents

Supplementary Note 1. Experimental setup

Our experiments include generating large-scale GHZ states and observing the phase oscillation of the GHZ state in the cat scar discrete time crystal (DTC). The first part is performed on two different quantum processors, labeled as I [1] and II [2], respectively. Processor I (II) is a two-dimensional (2D) flip-chip superconducting processor consisting of 121 (36) frequency-tunable transmon qubits and 200 (60) tunable couplers. The 121 (36) qubits are arranged as an 11×11 (6×6) square lattice and each nearest-neighbor (NN) qubit pair is connected by a tunable coupler in order to tune the NN coupling strength. Each processor is mounted on the mixing chamber plate of a dilution refrigerator (DR) with a temperature of ~20 mK (Supplementary Figure 1). Experimental setups for controlling and measuring the two processors are similar, which are illustrated in Supplementary Figure 1.

Supplementary Note 2. Device performance

We select 60 qubits (Supplementary Figure 2a) on Processor I to generate GHZ states due to limited wirings. For Processor II, all the 36 qubits are available and thus we can generate global entanglement across the whole device. Supplementary Figures 2a-f (g-l) display the basic performance of all the actively-used qubits on Processor I (II), including qubit idle frequency f_{10}, energy relaxation time T_1, spin echo dephasing time T_2^{SE}, single-qubit (SQ) gate cycle error, two-qubit CZ gate cycle error, and readout

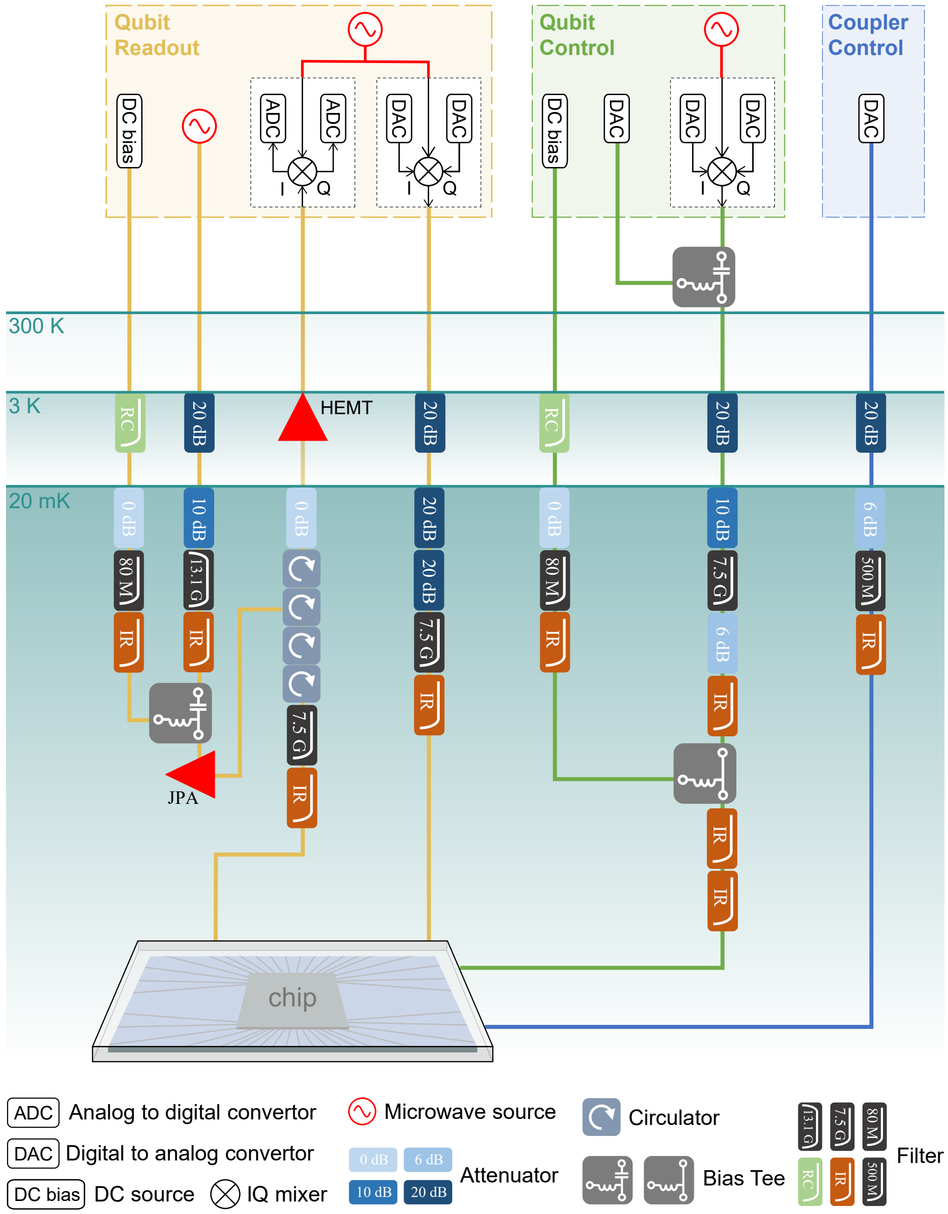

Supplementary Figure 1. **Illustration of experimental setup.** Room-temperature electronics for controlling and measuring qubits on the processor include three parts: coupler control (blue box), qubit control (green box) and readout (orange box). Fast Z control pulses for each qubit or coupler are generated with a single digital-to-analog converter (DAC) channel. Microwave pulses for either qubit readout or XY control are synthesized by mixing the local oscillator signal, generated by a microwave source, with two sideband signals generated by two DAC channels. DC bias outputs slow Z control pulses for biasing either the qubit idle frequencies or the operation frequencies of the Josephson parametric amplifiers (JPAs). All control pulses are transmitted through a series of attenuators and filters at different temperatures, for isolation of noises, before being injected into the flip-chip superconducting quantum processor, which is mounted on the mixing chamber plate of a dilution refrigerator.

fidelity. Notably, the average Pauli errors benchmarked with simultaneous cross entropy benchmarking (XEB) [3, 4] are 0.069% (0.203%) for single-qubit gates and 0.574% (0.543%) for two-qubit CZ gates on Processor I (II). We use single-qubit gates and two-qubit CZ gates to realize the parallel quantum circuits for generating GHZ state in Fig. 1a in the main text.

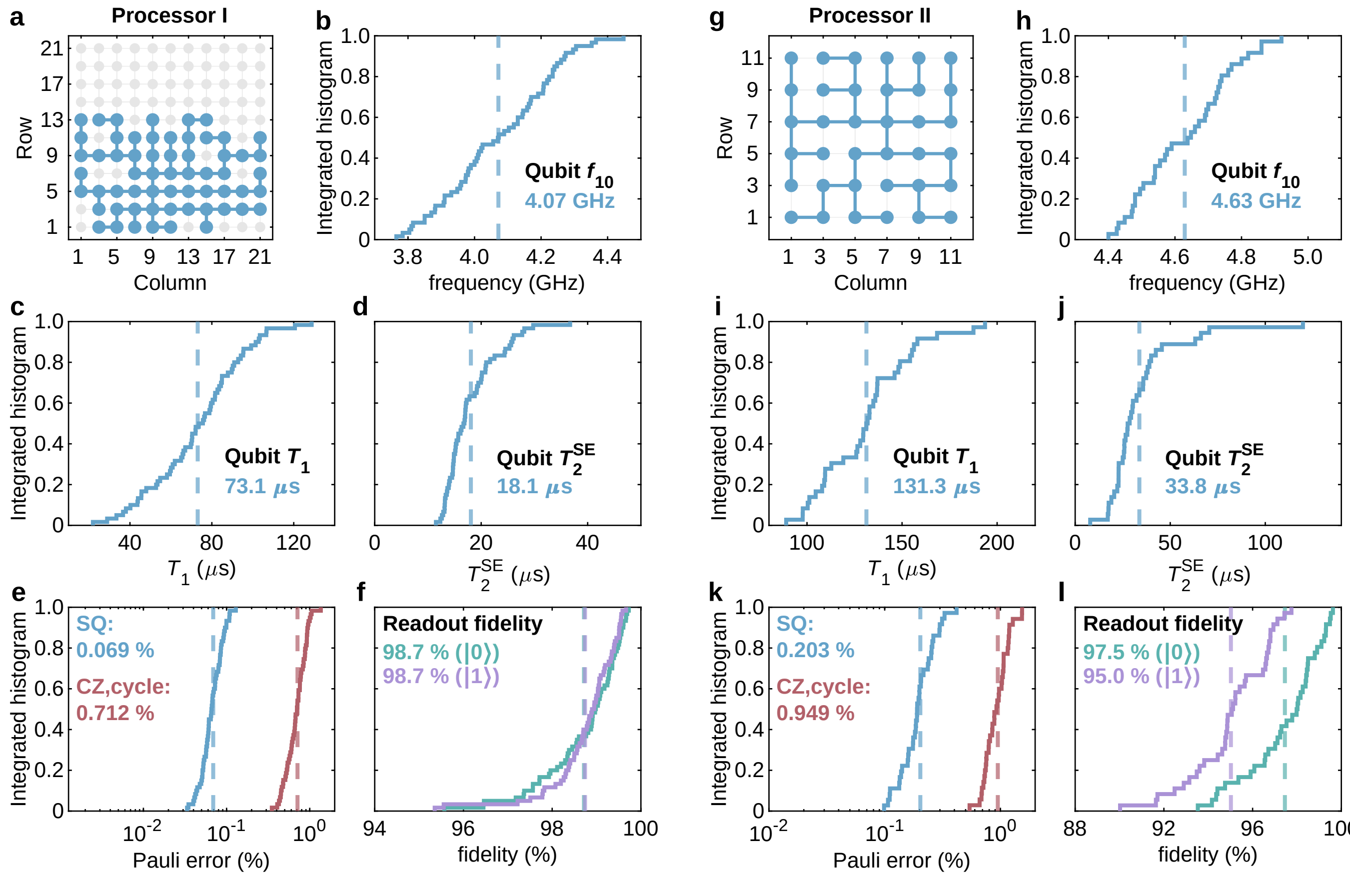

Supplementary Figure 2. **Device performance for Processor I (a-f) and Processor II (g-l).** **a**, **g**, Qubit layout for the two processors. Processor I (II) consists of an 11×11 (6×6) qubit array where we use up to 60 (36) qubits to generate GHZ states. Blue dots and lines denote the actively-used qubits and couplers for the generation of GHZ states, respectively. **b**, **h**, Distribution of qubit idle frequency f_{10}. **c**, **i**, Distribution of qubit relaxation time T_1 measured at the idle frequency. **d**, **j**, Distribution of qubit pure dephasing time T_2^{SE} measured with spin echo sequence at the idle frequency. **e**, **k**, Cycle Pauli error for single-qubit gates (blue line) and two-qubit CZ gates (red line) for generating GHZ states. Single-qubit errors are measured with XEB sequences running on 60 (36) qubits simultaneously for Processor I (II). For single-qubit XEB, a cycle only consists of one single-qubit gate. Two-qubit cycle errors are obtained by performing simultaneous XEB for each two-qubit layer in the GHZ state generation circuit, which is plotted in Supplementary Figure 4 (Supplementary Figure 5) for Processor I (II). During the simultaneous XEB for each two-qubit layer, those qubits that are not involved in CZ gates are also applied with single-qubit XEB sequences. For the two-qubit CZ gate, a cycle consists of one CZ gate and two single-qubit gates. **f**, **l**, Qubit readout fidelity for $|0\rangle$ (green line) and $|1\rangle$ (purple line). Vertical dashed lines in these panels denote the mean values.

Supplementary Note 3. GHZ states calibration

Multipartite entanglement plays a pivotal role in quantum information processing, serving as a crucial resource to speed up quantum algorithms [5] and realize error-correcting codes [6], etc. Among various entangled states, Greenberger-Horne-Zeilinger (GHZ) states are particularly significant since they possess global entanglement. However, they are also extremely vulnerable to noise, which makes the generation of large-scale GHZ states a formidable challenge. Experiment efforts on generating large-scale GHZ states verifying genuine multipartite entanglement with fidelity $\mathcal{F} > 0.5$ have been made in a range of quantum platforms including Rydberg atom arrays [7] (20 qubits), trapped ions [8, 9] (up to 32 qubits), photons [10] (18 qubits), and superconducting qubits [11, 12] (up to 27 qubits).

In our experiments, we exploit the 2D architecture of our superconducting quantum chips and design efficient digital quantum circuits to generate N-qubit GHZ states. Leveraging on the high-fidelity single- and two-qubit gates on our device (Supplementary Figure 2), we achieve a 60-qubit GHZ state with a fidelity $\mathcal{F} = 0.595 \pm 0.008$, unambiguously proving genuine multipartite entanglement with $\mathcal{F} > 0.5$.

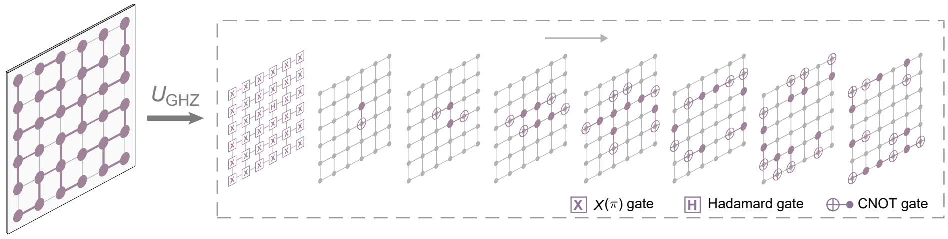

Supplementary Figure 3. **Illustration of the quantum circuit for generating the 36-qubit GHZ state on Processor II.** Left panel illustrates the radial path to build up entanglement, where purple dots and lines denote the actively-used qubits and couplers, respectively. Right panel bounded by dashed lines shows the full sequence of circuits to generate the anti-ferromagnetic GHZ state stepwise.

A. GHZ state generation circuits

The paradigmatic scheme to generate an N-qubit GHZ state $(|0101\ldots01\rangle + |1010\ldots10\rangle)/\sqrt{2}$ in one dimension follows a procedure starting from the Fock state $|0101\ldots01\rangle$: The first qubit is initialized to a superposition state $(1/\sqrt{2})(|0\rangle + |1\rangle) \otimes |101\ldots01\rangle$ by a Hadamard gate, after which a CNOT gate is applied to entangle it with its neighbor originally in $|1\rangle$ to produce the Bell state $(1/\sqrt{2})(|01\rangle + |10\rangle) \otimes |01\ldots01\rangle$; sequential CNOT gates are then applied to include more neighboring qubits one by one to achieve the global multipartite entanglement. The procedure described above is time-consuming, as it requires $N-1$ layers of CNOT gates to create an N-qubit GHZ state. However, since the qubits are arranged in 2D for our chips, each qubit can be entangled with more neighbors simultaneously and the circuit depth can be shortened. In this way, we generate the GHZ states using the protocols illustrated in Fig. 1a of the main text and Supplementary Figure 3, where the first single-qubit layer is designed to determine the spin pattern of the final GHZ state, and the following 9 (7) layers of CNOT gates build up the entanglement along a radial path for 60 (36) qubits.

In the experimental realization, we further compile these circuits using the experimentally accessible single- and two-qubit CZ gates on our processors. These gates are calibrated with high fidelities (see Supplementary Figures 2e and k), which makes it possible to generate sizable GHZ states with considerably high fidelities. The compiled circuit for generating the GHZ state of 60 (36) qubits on Processor I (II) is shown in Supplementary Figure 4 (Supplementary Figure 5), which contains 19 (15) physical circuit layers directly implemented for the state generation experiments.

B. Characterization of GHZ states

To obtain the fidelity of a GHZ state, we need to measure two diagonal and two off-diagonal terms of its density matrix (see Supplementary Eqs. (25) and (26)), from which we can calculate its fidelity. Typically, the fidelity $\mathcal{F} > 0.5$ witnesses the genuine N-particle entanglement [13]. The two diagonal terms can be obtained by directly measuring the population of the two composing Fock states (see Supplementary Figure 6). The two off-diagonal terms, which describe the quantum coherence between the two components, can be assessed by parity [13] or multiple quantum coherence (MQC) measurements [14, 15], with the latter being more suitable for systems equipped with digital gates, especially when the system size scales up. In this work, we adopt MQC to characterize the GHZ state (Fig. 1d of the main text). As a sanity check, we also benchmark the GHZ state fidelity by measuring the parity oscillations for the system size $N \leq 20$, with the results shown in Supplementary Figure 11.

1. Multiple quantum coherence (MQC)

MQC spectra are originally developed in nuclear magnetic resonance experiments [15] to characterize the many-body correlations. Its applications have been extended to probe out-of-time-order correlations [16], localization effects [17], and many-body entangled states [14]. MQC only requires measuring the ground state probability and thus is regarded as a scalable metric for experimentally verifying many-body entanglement [14]. Nevertheless, the protocol requires the implementation of additional reversed circuits to disentangle a GHZ state, which demands high-fidelity, versatile programmability, and long coherence time of quantum gates that can be satisfied by our system.

In the following, we employ the procedure in Ref. [14] as the main scheme to benchmark the macroscopic quantum coherence of the generated GHZ states, which we recapitulate below (the circuit is shown in Fig. 1c of the main text.)

1. Starting from N-qubit ground state $|00\ldots0\rangle$, we apply a quantum circuit U_{GHZ} (Supplementary Figure 3) to prepare the GHZ state: $U_{\mathrm{GHZ}}|00\ldots0\rangle = |\Phi, \boldsymbol{s}\rangle_N = \frac{1}{\sqrt{2}}(|0101\ldots01\rangle + e^{-\mathrm{i}\Phi}|1010\ldots10\rangle)$, where the spin pattern $\boldsymbol{s} = 0101\ldots01$.

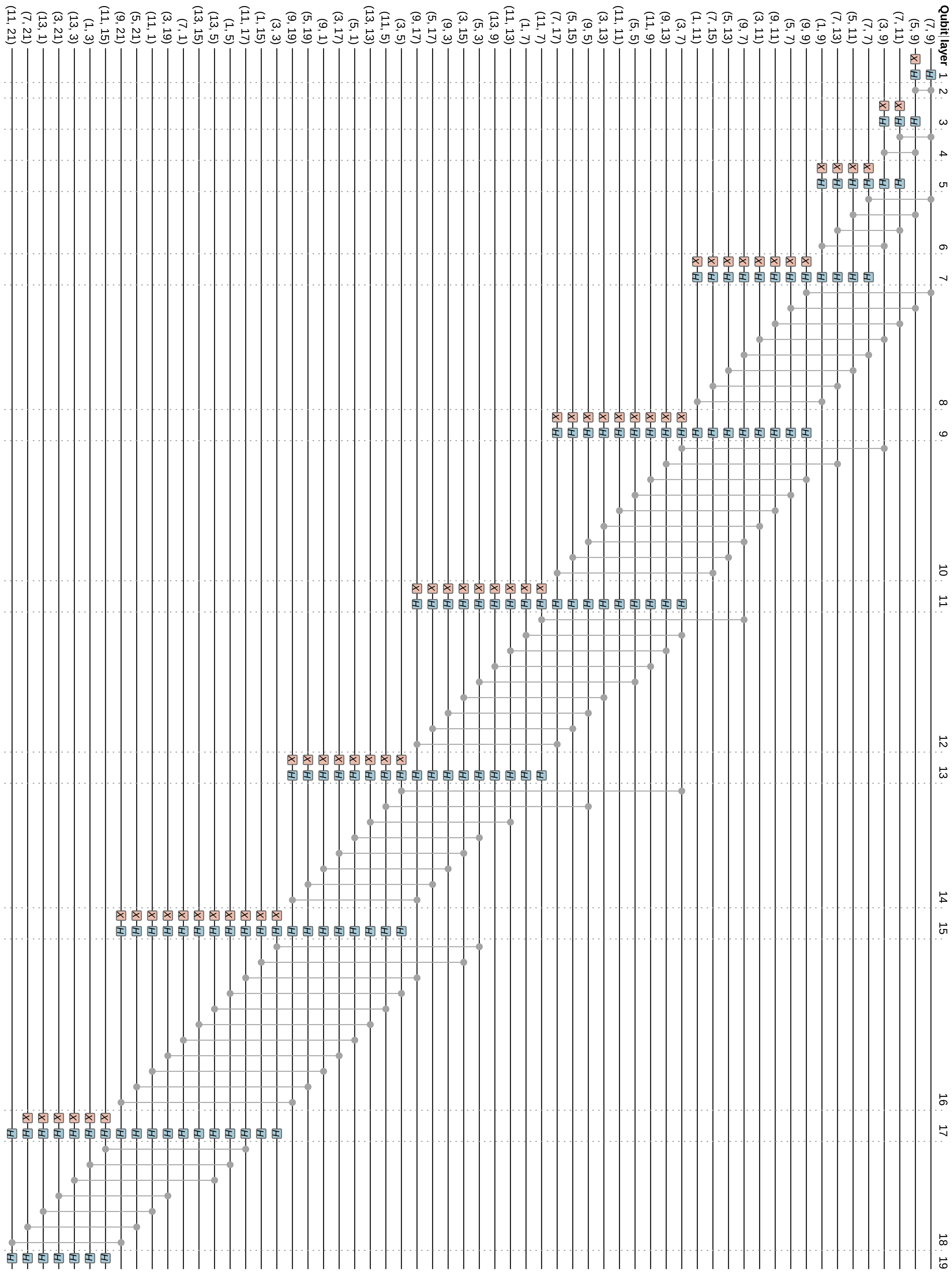

Supplementary Figure 4. **Experimental circuit for generating the 60-qubit GHZ state on Processor I.** This circuit diagram is obtained by compiling the circuit in Fig. 1a of the main text into single-qubit gates [$X(\pi)$, Hadamard gate] and two-qubit CZ gates. The whole circuit contains 19 layers, including 10 layers of parallel single-qubit gates and 9 layers of two-qubit gates. Each qubit is labeled by its column and row numbers according to the index map defined in Supplementary Figure 2a.

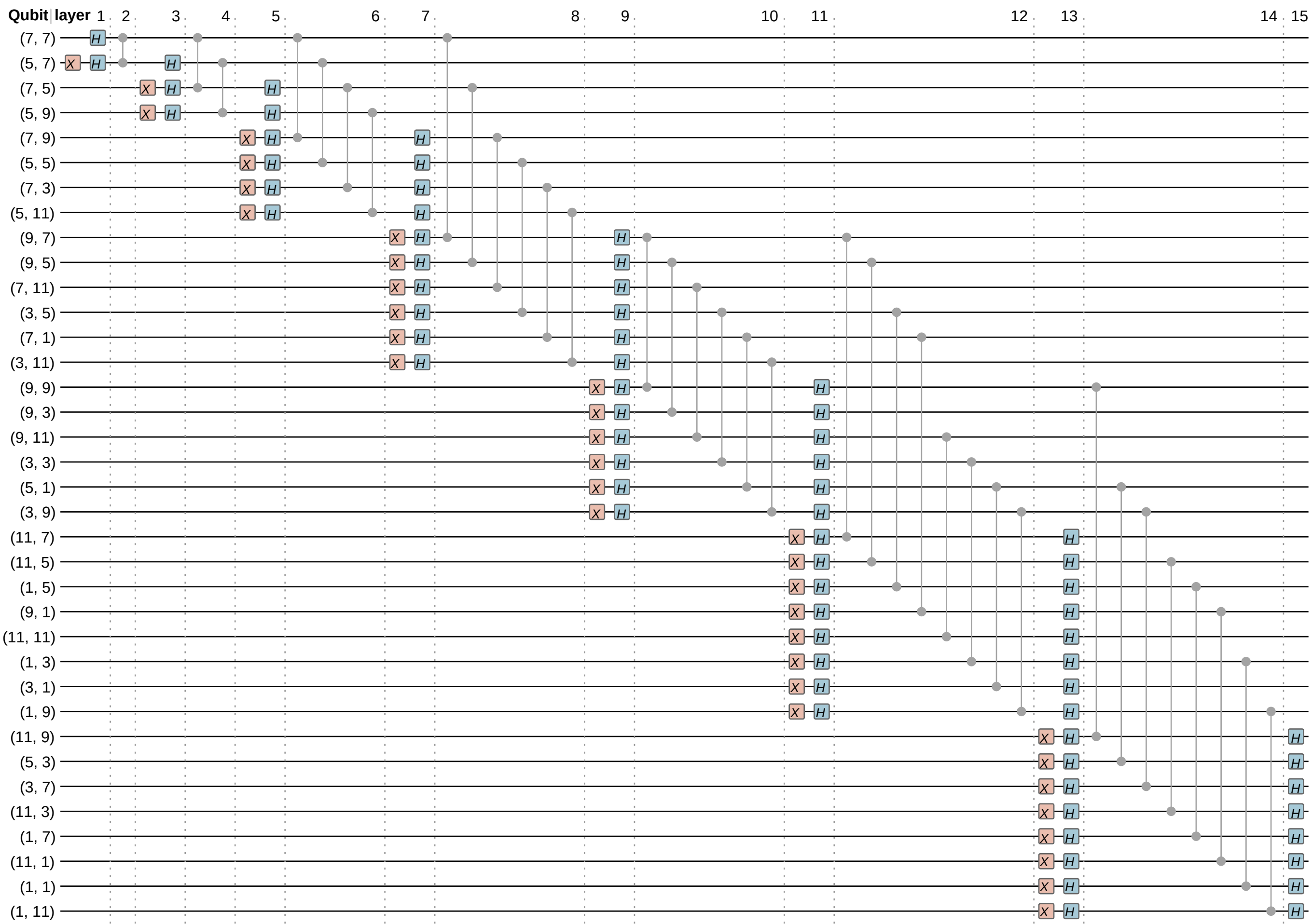

Supplementary Figure 5. **Experimental circuit for generating the 36-qubit GHZ state on processor II.** Similar to Supplementary Figure 4, this circuit is obtained by compiling the circuit in Supplementary Figure 3, which includes 8 layers of parallel two-qubit CZ gates and 7 layers of simultaneous single-qubit gates. Each qubit is labeled by its column and row numbers according to the index map defined in Supplementary Figure 2g.

2. For each qubit, we apply an $X(\pi)$ gate as the spin echo pulse to suppress the dephasing noise and a subsequent phase rotation ϕ (or $-\phi$) at the even (or odd) sites. The GHZ state then gains a collective phase as $|\Phi + N\phi, \boldsymbol{s}\rangle_N = \frac{1}{\sqrt{2}}(|0101\ldots01\rangle + e^{-\mathrm{i}(\Phi+N\phi)}|1010\ldots10\rangle)$.

3. We disentangle the GHZ state $|\Phi + N\phi, \boldsymbol{s}\rangle_N$ with a reversed circuit U_{GHZ}^{-1} and obtain $\frac{1}{\sqrt{2}}[(1 + e^{-iN\phi})|0\rangle + (1 - e^{-iN\phi})|1\rangle] \otimes |0000\ldots00\rangle$.

4. In the ideal case, the ground state probability $\mathcal{K}(\phi)$ is given by $\frac{1}{2}[1 + \cos(N\phi)]$.

$\mathcal{K}(\phi)$ can also be expressed by the following form

$$\mathcal{K}(\phi) = |\langle 00\ldots 0|U_{\mathrm{GHZ}}^{\dagger} U_Z(\phi) U_X U_{\mathrm{GHZ}}|00\ldots 0\rangle|^2 = \mathrm{Tr}(\rho(\phi)\rho), \tag{1}$$

where $U_Z(\phi) = \prod_{j=1}^{N} Z_j[(-1)^{s_j}\phi]$, $U_X = \prod_{j=1}^{N} X_j(\pi)$, $\rho = |\Phi, \boldsymbol{s}\rangle_{NN}\langle\Phi, \boldsymbol{s}|$, $\rho(\phi) = U_Z(\phi) U_X \rho U_X^{\dagger} U_Z^{\dagger}(\phi)$. The density matrix ρ can be written into blocks as $\rho = \sum_{m_s, m_{s'}} \rho_{m_s, m_{s'}} |m_s\rangle\langle m_{s'}| = \sum_q \rho_q$, where $\rho_q = \sum_{m_s} \rho_{m_s, m_s - q} |m_s\rangle\langle m_s - q|$, $m_s = \sum_j s_j$, and $|\boldsymbol{s}\rangle = |s_j\rangle^{\otimes N}$. Due to $U_Z(\phi)\rho_q U_Z(\phi)^{\dagger} = e^{iq\phi}\rho_q$ and $U_X \rho_q U_X^{\dagger} = \rho_{-q}$, we have

$$\mathcal{K}(\phi) = \mathrm{Tr}(\rho(\phi)\rho) = \mathrm{Tr}(\sum_q e^{iq\phi}\rho_{-q} \sum_p \rho_p) = \sum_q e^{iq\phi}\mathrm{Tr}(\rho_{-q}\rho_q). \tag{2}$$

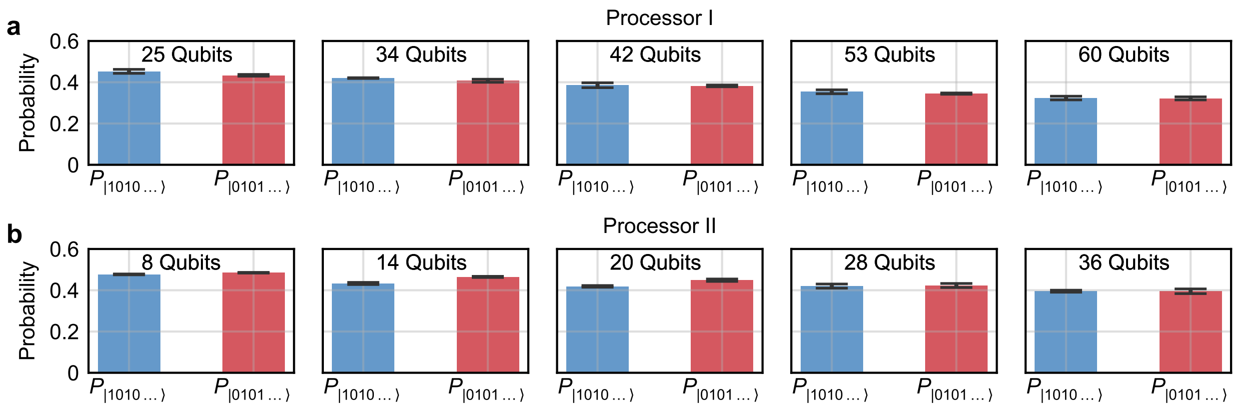

Supplementary Figure 6. **Diagonal terms of GHZ states for different system sizes.** **a** and **b** are the measured diagonal terms $P_{|1010...\rangle}$ and $P_{|0101...\rangle}$ on processor I and II, respectively. Data with error bars are repeatedly measured five times and error bars stem from their standard deviations.

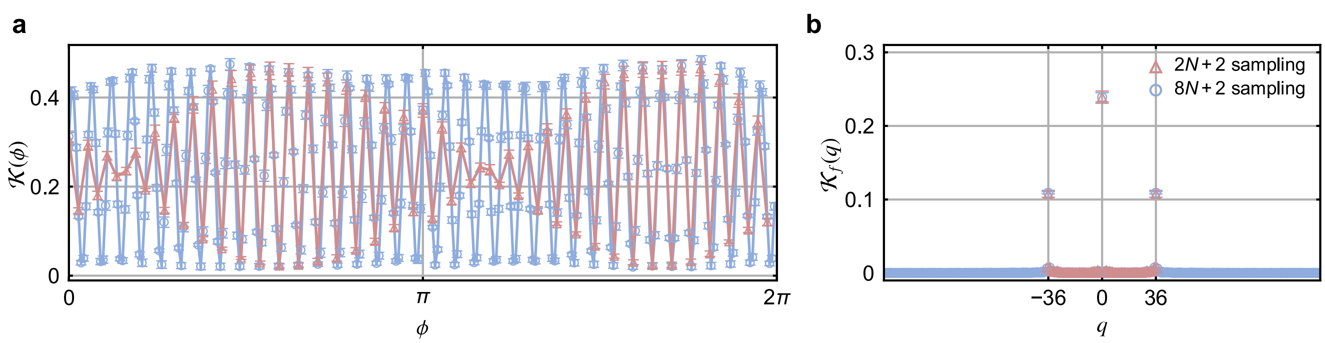

Supplementary Figure 7. **Effect of sampling size on MQC spectra–sparse sampling vs. dense sampling.** **a**, Experimentally measured $\mathcal{K}(\phi)$ for the 36-qubit GHZ state. Red triangles denote the results by the sparse sampling of $2N+2$ points, and blue circles show those obtained by the dense sampling with $8N+2$ points. **b**, Fourier spectra of $\mathcal{K}(\phi)$.

By performing the discrete Fourier transformation to the experimentally measured $\mathcal{K}(\phi)$, we can obtain $\mathcal{K}_f(q) = \mathcal{N}_s^{-1}|\sum_\phi e^{iq\phi}\mathcal{K}(\phi)|$, where the normalization constant $\mathcal{N}_s$ is the sampling number of ϕ. Thus, the off-diagonal term of the GHZ state $|\rho_{0101...,1010...}|^2 = \mathrm{Tr}(\rho_N\rho_{-N}) = \mathrm{Tr}(\rho_N\rho_N^\dagger)$ is given by $\mathcal{K}_f(N)$.

To accurately measure $\mathcal{K}_f(N)$ without sacrificing the efficiency, we follow the convention of Ref. [14] and measure $\mathcal{K}(\phi)$ with a sparse sampling on ϕ with $\phi = \frac{\pi j}{N+1}$ $(j = 0, 1, 2, ..., 2N+1)$. We compare the results of sparse sampling ($\mathcal{N}_s = 2N+2$) with a dense one ($\mathcal{N}_s = 8N+2$) for the 36-qubit GHZ state, which are shown in Supplementary Figure 7. In spite of less sample points for ϕ (Supplementary Figure 7b), the measured MQS spectra $\mathcal{K}_f(q)$ for sparse sampling $\mathcal{N}_s = 2N+2$ match well with that of $\mathcal{N}_s = 8N+2$. They show almost the same peak value at $q = 36$, which signifies the existence of the N-particle entanglement for the prepared GHZ state. Therefore, we can safely measure the $\mathcal{K}(\phi)$ signals by sampling $2N+2$ points ($\phi = \frac{\pi j}{N+1}$, $j = 0, 1, 2, ..., 2N+1$) in our experiments. For each $\mathcal{K}(\phi)$, we take 60,000 measurement shots on Processor I and 72,000 shots on Processor II. Since MQC only requires measuring the ground state probabilities, readout errors occur mostly in the low-excitation subspace, which enables us to correct the measurement errors in a scalable way [14]. We rank the Fock bases according to their measured raw probabilities from high to low, and pick up the first 256 Fock bases for readout corrections. The measured $\mathcal{K}(\phi)$ after readout correction and its Fourier spectra $\mathcal{K}_f(q)$ are shown in Supplementary Figure 8 for Processor I and Supplementary Figure 9 for Processor II. In addition, we use the same readout correction scheme to eliminate readout errors in measuring diagonal terms P_s, $P_{\bar{s}}$.

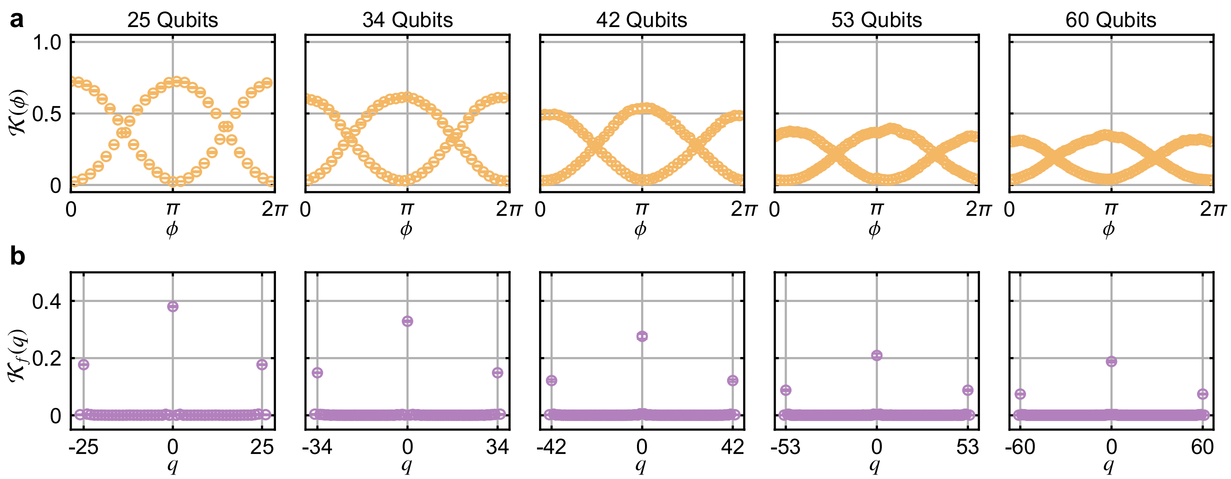

Supplementary Figure 8. **MQC results for different system sizes on processor I. a**, Experimentally measured $\mathcal{K}(\phi)$. **b**, Amplitudes of the Fourier spectrum for $\mathcal{K}(\phi)$. The highest three peaks appear at $q = 0$ and $q = \pm N$, where N is the number of qubits. The absolute value of the major off-diagonal elements for the GHZ states can be calculated by the Fourier amplitude $\mathcal{K}_f(q = N)$.

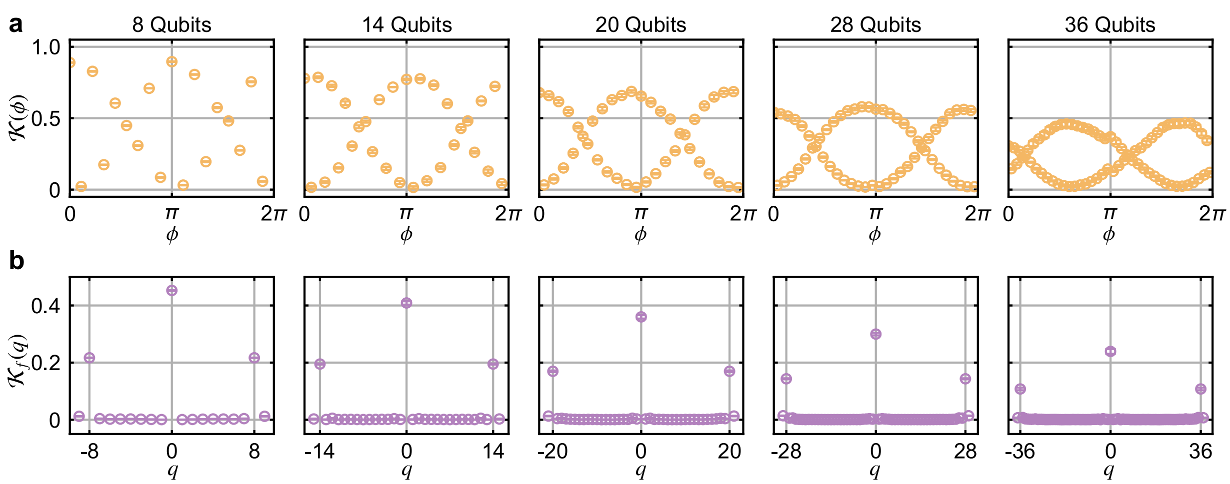

Supplementary Figure 9. **MQC results for different system sizes on processor II. a**, Experimentally measured $\mathcal{K}(\phi)$. **b**, Amplitudes of the Fourier spectrum for $\mathcal{K}(\phi)$. The highest three peaks appear at $q = 0$ and $q = \pm N$, where N is the number of qubits. The absolute value of the major off-diagonal elements for the GHZ states can be calculated from the MQC amplitude $\mathcal{K}_f(q = N)$.

2. *Parity oscillations*

Parity oscillations have been widely used to measure the off-diagonal terms of GHZ states [7, 10, 11, 13, 18, 19]. Parity $\mathcal{P}(\gamma)$ of a GHZ state $\frac{1}{\sqrt{2}}(|0101\ldots\rangle + \exp(i\Phi)|1010\ldots\rangle)$ for an even qubit number is given by

$$\langle\mathcal{P}(\gamma)\rangle = \langle\otimes_{j=1}^{N}(-1)^j\left[\cos((-1)^j\gamma)\sigma_j^y + \sin((-1)^j\gamma)\sigma_j^x\right]\rangle = (-1)^{N/2} \times 2|\rho_{0101\ldots,1010\ldots}|\cos(N\gamma + \Phi), \tag{3}$$

where γ is the rotation angle. $\mathcal{P}(\gamma)$ is an N-body operator involving the probabilities of a large number of Fock bases, which requires a significantly large number of measurement shots and limits the size of the system that can be characterized. Therefore, as a cross-validation, we characterize the Bell state and the GHZ states for small system sizes with $N = 4, 8, 14, 20$. The measured results are illustrated in Supplementary Figure 10, where we conduct about 2^{20}, 30000, 6000 measurement shots for system sizes of $N = 20$, $N = 14$, and $N < 14$, respectively. Because the probabilities can be distributed over the whole Fock basis of the Hilbert space for measuring the parity, we cannot truncate the number of the basis to eliminate the measurement errors. Here, instead, we apply the full readout correction matrix to the raw probabilities [11, 20] for the parity measurements, which is a tensor product of the measured single-qubit correction matrices.

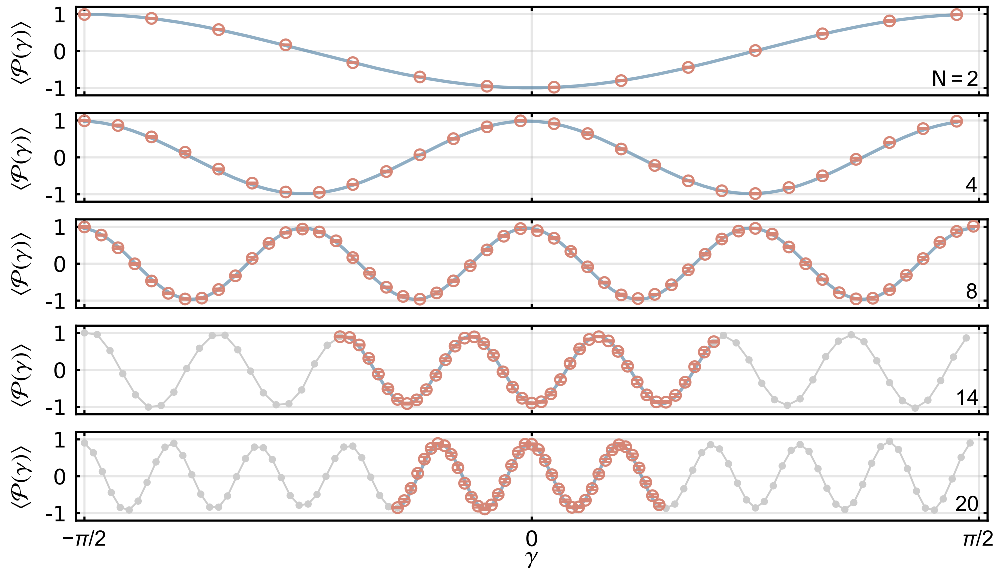

Supplementary Figure 10. **Parity oscillations.** Measured $\langle\mathcal{P}\rangle$ on Processor II for the bell state and the GHZ states of 4, 8, 14, and 20 qubits. Data with error bars (orange dots) are repeatedly measured five times and error bars stem from their standard deviations, while gray dots connected by gray lines are experimental data measured only once. Blue lines are fitted with the function $(-1)^{N/2} \times A\cos(N\gamma + C)$.

C. Numerical results

We numerically simulate the generation of the GHZ states using Monte Carlo wavefunction method [21, 22]. In the simulation, error operations are applied following each quantum gate, with probabilities determined by their noise models. The expectation value of an observable is obtained by averaging over the outcomes of an ensemble of noisy quantum circuits. Here, the numerical simulation is performed using MindSpore Quantum [23], which is an open-source quantum computation framework.

We simulate the fidelity scaling of the GHZ states on Processor II for $N \leq 20$. Note that there are 7 layers of CZ gates in our circuit (Supplementary Figure 5) for generating 36-qubit GHZ states. For simulating a N-qubit GHZ state, we consider the depolarization, energy relaxation, and dephasing as our noise models. The error rates of the depolarization model for different system sizes are listed in Supplementary Table 1, which are assessed based on the experimentally measured gate errors subtracting the contribution of the decoherence errors. The error rates of the energy relaxation and dephasing models are calculated based on the average energy relaxation time T_1 (Supplementary Figure 2j), dephasing time T_2^{SE} (Supplementary Figure 2i), and gate length (24 ns single-qubit gate and 60 ns two-qubit gate). Supplementary Figure 11 shows the comparison between the experimental results and the numerical simulations. Numerical simulations agree well with the experimental GHZ fidelities measured with parity method. Note that experimentally measured GHZ fidelities with MQC show a lower fidelity than parity method due to extra gate errors and decoherence errors introduced by the imperfect reversal unitary.

Qubit number N	2	4	8	14	20
number of CZ layers	1	2	3	4	5
e_p of single-qubit gates (%)	0.049	0.031	0.045	0.064	0.056
e_p of CZ gates (%)	0.256	0.148	0.199	0.225	0.227

Supplementary Table 1. Gate errors for simulating GHZ states.

Supplementary Note 4. Realization of a cat scar DTC

A. Digital circuit of DTC

To realize a perturbed Ising model of periodical boundary described by equation (2) of the main text, we construct a 36-qubit ring on Processor II (Supplementary Figure 12a). The quantum circuit to realize a cycle of the Floquet unitary U_{F} is shown

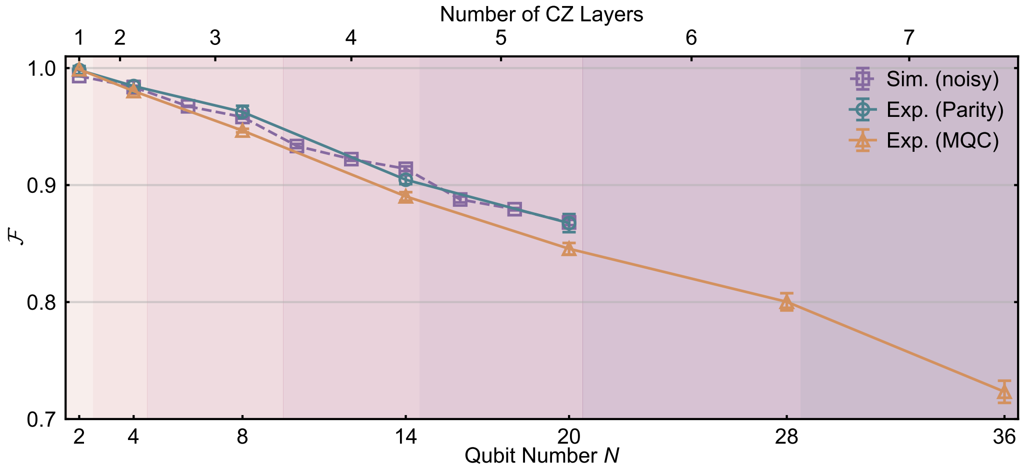

Supplementary Figure 11. **GHZ state fidelity on Processor II – experiment vs. simulation.** Experimentally measured fidelities of GHZ states are obtained using parity (circles) and MQC (triangles) methods. Numerical results (dashed lines with squares) are obtained with the Monte Carlo wavefunction method. Colored backgrounds indicate the number of CZ layers for different system sizes. Numerical results are averaged over 30, 000 random samples of noise realizations for good convergence. Experimental (numerical) error bars correspond to the standard deviations of five repetitions of measurements (five random seeds to generate random noise samples).

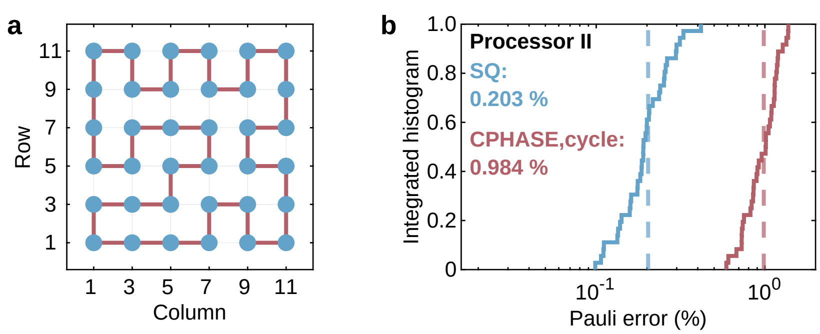

Supplementary Figure 12. **Realization of an Ising ring.** **a**, Construction of a 36-qubit Ising ring on Processor II. Blue dots denote qubits, which emulate the spins. Red lines represent tunable couplers, which realize Ising interactions between spins. **b**, Cycle Pauli errors of single-qubit gates and CPHASE(-4) gates, which are obtained by performing simultaneous XEB for each layer in the DTC circuits.

in Fig. 2c of the main text, which includes two kinds of gates, $U3(\alpha,\beta,\gamma)$ and $ZZ(-4)$. $U3(\alpha,\beta,\gamma)$ is a single-qubit rotation parameterized with three Euler angles, given by

$$U3(\alpha,\beta,\theta)=\begin{pmatrix}\cos\left(\frac{\alpha}{2}\right) & -ie^{-i\beta}e^{i\theta}\sin\left(\frac{\alpha}{2}\right)\\ -ie^{i\beta}\sin\left(\frac{\alpha}{2}\right) & e^{i\theta}\cos\left(\frac{\alpha}{2}\right)\end{pmatrix}=\begin{pmatrix}1 & 0\\ 0 & e^{i\theta}\end{pmatrix}\begin{pmatrix}\cos\left(\frac{\alpha}{2}\right) & -ie^{-i(\beta-\theta)}\sin\left(\frac{\alpha}{2}\right)\\ -ie^{i(\beta-\theta)}\sin\left(\frac{\alpha}{2}\right) & \cos\left(\frac{\alpha}{2}\right)\end{pmatrix}. \tag{4}$$

$U3(\alpha,\beta,\gamma)$ gate is realized by a microwave pulse, which rotates qubit state around $(\beta-\theta)$-axis in the xy plane by an angle α, and a subsequent virtual phase gate $Z(\theta)$. Two layers of two-qubit $ZZ(\phi)$ gates emulate the Ising interactions on the chain, which are realized by a controlled ϕ-phase gate [CPHASE(ϕ)] and two single-qubit phase rotations

$$ZZ(\phi)=e^{i\frac{\phi}{4}Z_jZ_k}=Z_j(-\phi/2)Z_k(-\phi/2)\mathrm{CPHASE}(\phi). \tag{5}$$

Note that CZ gate used in preparing GHZ state is a CPHASE(ϕ) gate with $\phi=\pi$.

In our experiments, we set interaction strength $J=1$ and cycle period $T=1$, thus, the controlled phase $\phi=-4JT=-4$. Two single-qubit rotations, $U3(\alpha,\beta,\gamma)$ and $U3'(\alpha',\beta',\gamma')$ encode single-qubit Rabi drives and the generic perturbations in U_{F}, whose mapping to the parameters φ_1,φ_2, λ_1, and λ_2 in U_{F} are given in Supplementary Note 5B. We experimentally benchmark single-qubit gates and two-qubit CPHASE(-4) gates with simultaneous XEB sequences, with the measured Pauli errors per cycle shown in Supplementary Figure 12b.

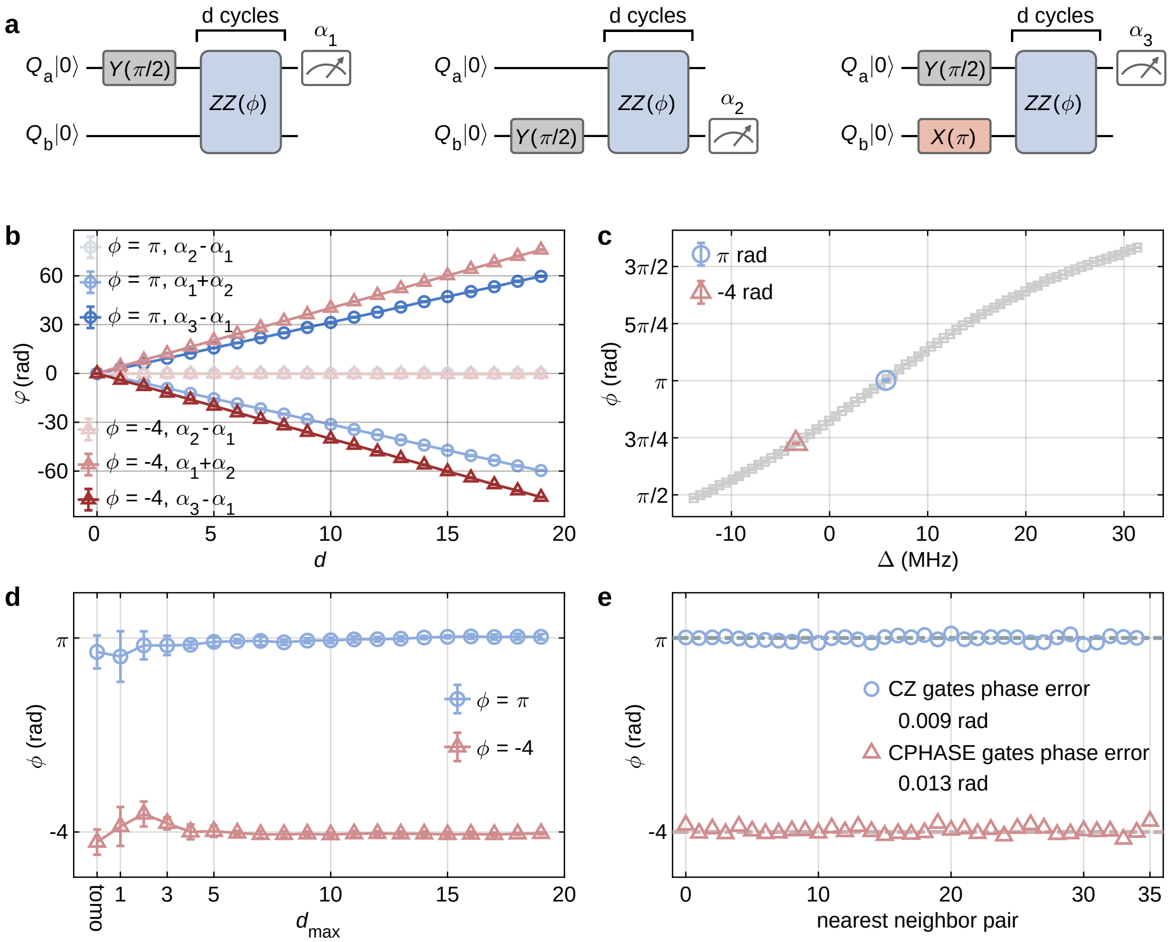

Supplementary Figure 13. **Calibration of Floquet circuits. a**, Quantum circuits for calibrating α_1, α_2, and α_3. **b**, Experimental results of the calibrated α_1, α_2, and α_3 for $\phi = \pi$ (red) and $\phi = -4$ (blue) as functions of cycle d. Markers are experimental results and lines are linear fits. **c**, Measured controlled phase ϕ as a function of detuning Δ. **d**, Convergence of ϕ with the increase of the maximum cycle d_{max} for $\phi = \pi$ (blue) and $\phi = -4$ (red). **e**, Measured controlled phase ϕ for the gates used in our experiments. Dashed lines indicate the target controlled phase. Marks are experimental results.

B. CPHASE gate calibration

We implement two-qubit CPHASE(ϕ) gates by tuning the coupling strength between qubits [24]. In the general case, the tunable couplers allow us to realize a Fermionic Simulation gate [25], which is given by

$$\begin{pmatrix} 1 & 0 & 0 & 0 \\ 0 & e^{i(\Delta_+ + \Delta_-)}\cos\theta & -ie^{i\left(\Delta_+ - \Delta_{-,\mathrm{off}}\right)}\sin\theta & 0 \\ 0 & -ie^{i\left(\Delta_+ + \Delta_{-,\mathrm{off}}\right)}\sin\theta & e^{i(\Delta_+ - \Delta_-)}\cos\theta & 0 \\ 0 & 0 & 0 & e^{i(2\Delta_+ + \phi)} \end{pmatrix}, \tag{6}$$

where ϕ is the controlled phase on $|11\rangle$, θ is the swap angle between $|01\rangle$ and $|10\rangle$ [$\theta = 0$ for CPHASE(ϕ) gate], and Δ_+,Δ_- and $\Delta_{-,\mathrm{off}}$ are single-qubit phases. In our experiments, we needs CPHASE(ϕ) gates with two specific angles, -4 (ZZ interaction) and π (CZ gate). We use Floquet calibration method [26, 27] to tune up the parameters ϕ, Δ_+, and Δ_- to realize a target CPHASE(ϕ) gate. The controlled phase ϕ and single-qubit phases Δ_+, Δ_- are calibrated using periodic circuits sharing a similar structure as shown in Supplementary Figure 13a. We initialize one qubit along the x-axis of the Bloch sphere and keep the other one in $|0\rangle$ or $|1\rangle$ state. d cycles of $ZZ(\phi)$ gates are then applied to improve the sensitivity. Finally, we perform tomographic measurements on the first qubit and obtain $\alpha = \arctan(\langle Y\rangle/\langle X\rangle)$. In the case of $\theta \approx 0$,we can extract these phases by $\alpha_1 + \alpha_2 = 2\Delta_+ d$, $\alpha_2 - \alpha_1 = 2\Delta_- d$, $\alpha_3 - \alpha_1 = \phi d$. Whereas the measured phase may be not accurate for each sequence with a specific d, we can estimate it more faithfully by fitting the accumulated phase as a function of the cycle d (Supplementary Figure 13b). As shown in Supplementary Figure 13d, as d_{max} ($d = 1, 2, ..., d_{\mathrm{max}}$) increases, the fitted ϕ converges to a stable value. The controlled phase

ϕ depends on the detuning Δ ($f_{10} - f_{21}$) of the two qubits. We carefully calibrate ϕ with $d_{\max} = 20$ for each Δ. As shown in Supplementary Figure 13c, we can control ϕ in a range of $[\pi/2, 3\pi/2]$ by tuning Δ. We show the calibrated values of ϕ for CZ gate ($\phi = \pi$) and CPHASE(-4) gate in Supplementary Figure 13e. The average phase error is ~ 0.01 rad.

Supplementary Note 5. Theoretical details and additional experimental data

A. General scheme of engineering cat eigenstates and comparison of different DTCs

Discrete time crystals (DTCs) are featured by a rigid reduced periodicity $nT, n \geqslant 2 \in \mathbb{Z}$ for the oscillation of physical observables, compared with driving period T. Such a phenomenon fulfills the concept of spontaneous breaking of discrete time translation symmetry. Here, for our purpose of protecting and controlling GHZ states, we focus on a particular class of DTCs that can host pairwise cat eigenstates, which are catalyzed by Ising interactions and global spin-flip pulses. The functionality of these two driving terms can be most intuitively understood at the unperturbed anchor point

$$U_F^{(0)} = U_2^{(0)} U_1^{(0)}, \qquad \text{Ising: } U_2^{(0)} = e^{-i\sum_{j,k} J_{jk}\sigma_j^z\sigma_k^z}, \quad \text{spin-flip: } U_1^{(0)} = e^{-i\pi\sum_{j=1}^N(\sigma_j^x/2)} = (-i)^N \prod_{j=1}^N \sigma_j^x. \tag{7}$$

Here, $\sigma_j^{x,y,z}$ are Pauli operators acting on a spin-1/2 state $|s_j\rangle$ at site $j = 1, 2, \ldots, N$, where $s_j = 1, 0$ for spin $\uparrow, \downarrow$. In the Floquet operator $U_F^{(0)}$, Ising interaction in $U_2^{(0)}$ structures the eigenstates as Fock states,

$$|\boldsymbol{s}\rangle \equiv |s_1 s_2 \ldots s_N\rangle, \qquad\qquad U_2^{(0)}|\boldsymbol{s}\rangle = e^{-iE_{\text{Ising}}(\boldsymbol{s})T}|\boldsymbol{s}\rangle, \tag{8}$$

with Ising interaction energy $E_{\text{Ising}}(\boldsymbol{s}) = \sum_{jk} J_{jk}(2s_j - 1)(2s_k - 1)$. Importantly, two opposite Fock states $|\boldsymbol{s}\rangle$ and $|\bar{\boldsymbol{s}}\rangle \equiv \prod_{j=1}^N \sigma_j^x|\boldsymbol{s}\rangle = |(1-s_1)(1-s_2)\ldots(1-s_N)\rangle$ share the same $E_{\text{Ising}}(\boldsymbol{s}) = E_{\text{Ising}}(\bar{\boldsymbol{s}})$ and form a degenerate doublet. Then, the global spin-flip pulse $U_1^{(0)}|\boldsymbol{s}\rangle \propto |\bar{\boldsymbol{s}}\rangle$ lifts the degeneracy and generates cat eigenstates,

$$|\Phi_\pm, \boldsymbol{s}\rangle = \frac{|\boldsymbol{s}\rangle + e^{i\Phi_\pm}|\bar{\boldsymbol{s}}\rangle}{\sqrt{2}}; \qquad U_F|\Phi_\pm, \boldsymbol{s}\rangle = (-i)^N e^{-i(E_{\text{Ising}}(\boldsymbol{s}) + \Phi_\pm)T}|\Phi_\pm, \boldsymbol{s}\rangle, \quad \Phi_+ = 0,\ \Phi_- = \pi/T. \tag{9}$$

Two cat eigenstates in the same Fock subspace $|\Phi_+, \boldsymbol{s}\rangle, |\Phi_-, \boldsymbol{s}\rangle$ are separated by a large quasienergy gap $\Phi_- - \Phi_+ = \pi/T$.

The relation between cat eigenstate pairs and previous experiments on DTCs can be illustrated below. Consider an initial state $|\boldsymbol{s}\rangle$, which simultaneously overlaps with both cat eigenstates $|\Phi_\pm, \boldsymbol{s}\rangle$. This Fock state will alternate between $|\boldsymbol{s}\rangle$ and $|\bar{\boldsymbol{s}}\rangle$ during evolution with period $2T$ due to π/T spectral gap, corresponding to magnetic order oscillations in experiments. Nevertheless, a subtle issue is whether the observed magnetic order oscillation is attributable to slow-relaxation in diffusive systems or to localized cat eigenstates [28]. To distinguish the two scenarios, recent DTC experiments have measured two-body correlations in addition to one-body magnetic orders [27, 29]. Alternatively, GHZ states generated in this work offer a unique N-body observable, the macroscopic quantum coherence, to directly benchmark the underlying cat eigenstates.

Focusing on cat eigenstate engineering, a crucial question is how robust are these cat eigenstates facing perturbations. To quantify the robustness, for generic Floquet eigenstates $|\epsilon_m\rangle$, $U_F|\epsilon_m\rangle = e^{i\epsilon_m}|\epsilon_m\rangle$, we exploit the inverse participation ratio (IPR)

$$\text{IPR}_m = \sum_{\boldsymbol{s}} |\langle \boldsymbol{s}|\epsilon_m\rangle|^4. \tag{10}$$

A larger value of IPR corresponds to stronger localization in Fock space and indicates better quality of a cat eigenstate. For instance, ideal cat eigenstates in Supplementary Eq. (9) takes the IPR value 1/2. Contrarily, an eigenstate in the ergodic limit with equal amplitudes on all Fock states $|\epsilon_m\rangle = (1/\sqrt{2^N})\sum_{\boldsymbol{s}}|\boldsymbol{s}\rangle$ gives vanishing $\text{IPR}_m = 1/2^N \to 0$ as the system size N grows.

To date, three mechanisms to stabilize cat eigenstates against perturbations have been proposed, namely, many-body localization, prethermalization with Landau's symmetry breaking, and cat scars. They chiefly differ in the Ising interactions employed, which result in different number and type of robust cat eigenstates as summarized in Supplementary Table 3. For unified comparison, we consider a model similar to Eq. (2) in the main text,

$$\begin{aligned} &U_F = U_2(\lambda_2)U_1(\lambda_1), \qquad U_1(\lambda_1) = U_P(\varphi_1, \lambda_1, \varphi_2)e^{-i\pi\sum_{j=1}^N(\sigma_j^x/2)}, \qquad U_2(\lambda_2) = e^{-iT\sum_{j=1}^N J_{jk}\tilde{\sigma}_j^z(\lambda_2)\tilde{\sigma}_k^z(\lambda_2)}, \\ &U_P(\varphi_1, \lambda_1, \varphi_2) = \prod_{j=1}^N e^{-i\varphi_1\sigma_j^z/2}e^{i\lambda_1\sigma_j^y/2}e^{-i\varphi_2\sigma_j^z/2}, \qquad \tilde{\sigma}_j^z(\lambda_2) = \cos(\lambda_2)\sigma_j^z + \sin(\lambda_2)\sigma_j^x. \end{aligned} \tag{11}$$

Perturbing terms	Purpose of introducing such terms	Parameter range
Single-spin perturbation $e^{i\lambda_1\sigma_j^y/2}$	Check whether DTC is robust against spin-flips trying to delocalize cat eigenstates and detune the period-$2T$ oscillation	$\lambda_1 \ll J \sim 1$
Two-spin perturbation $e^{-i(\sim\sigma_j^z\sigma_{j+1}^x,\sigma_j^x\sigma_{j+1}^z,\sigma_j^x\sigma_{j+1}^x)}$	Transverse interactions to accelerate relaxation and make sure the observed DTC effects represent a steady state	$\lambda_2 \ll J \sim 1$
Longitudinal fields $e^{-i\varphi_1\sigma_j^z/2}$, $e^{-i\varphi_2\sigma_j^z/2}$	Introduce two such terms to solve the dilemma that longitudinal fields should be strong to break integrability, but not to accidentally induce fine-tuned spin echos that interfere with checking DTC robustness by other terms	Strong $\varphi_1, \varphi_2 \sim 1$ to break integrability and avoid echo $\lvert\varphi_1 - \varphi_2\rvert = 0$

Supplementary Table 2. Motivation of introducing each term and the associated parameter choices.

Here, to test the robustness of cat eigenstates against generic perturbation, we add to Supplementary Eq. (7) both single-qubit and two-qubit perturbations parameterized by $\lambda_1, \lambda_2 \ll 1$ respectively. Two longitudinal fields φ_1, φ_2 are adopted to ensure both breaking the integrability of the model and avoiding single-qubit echoes that may interfere with the benchmark of many-body effects. For clarity, the effects of these perturbing terms are summarized in Supplementary Table 2. These perturbations are chosen to be the same for all three cases as specified in the first column of Supplementary Table 3. On the other hand, different Ising interactions J_{jk} prescribe three distinct regimes listed in the second to fourth columns in Supplementary Table 3.

1. **Many-body localization (MBL).**
   In DTCs, the global qubit flip $e^{-i\pi\sum_j(\sigma_j^x/2)} = (-i)^N \prod_{j=1}^N \sigma_j^x$ can largely cancel the effect of hypothetical random longitudinal fields, i.e., $h_j^z\sigma_j^z$, that are often exploited to engineer MBL, because in every two periods $U_F^2 \sim \prod_j \sigma_j^x e^{-i\sum_j h_j^z\sigma_j^z} \prod_j \sigma_j^x e^{-i\sum_j h_j^z\sigma_j^z} \propto$

mechanisms	many-body localization	prethermalization with Landau's symmetry breaking	**cat scars**
Conditions of Ising interaction $e^{-iT\sum_{jk}J_{jk}\sigma_j^z\sigma_k^z}$	1, Disordered *interaction* $J_{j,j+1} \in [J - \frac{W}{2}, J + \frac{W}{2}]$, $(JT, WT \sim 1)$ needed, as spin π-pulse $e^{-i\pi\sum_j(\sigma_j^x/2)}$ cancels longitudinal fields every two periods 2, 1D with short-range interaction	1, High frequency driving $J_{jk}T \ll 1$ for prethermal lifetime $\sim e^{1/J_{jk}T}$, and weak perturbation $\lambda < J_{jk}$ for ordering 2, In 1D, long-range interaction is needed to circumvent the instability predicted by Mermin-Wagner theorem	With strong interaction $JT \sim 1$ and the signs $J_{j,j+1} = (2s_j - 1)(2s_{j+1} - 1)J$, two pairs of scars are engineered as $\lvert s_1 s_2 \ldots\rangle \pm e^{-i\gamma}\lvert\bar{s}_1\bar{s}_2\ldots\rangle$ and $\lvert s_1\bar{s}_2\ldots\rangle \pm e^{+i\gamma'}\lvert\bar{s}_1 s_2\ldots\rangle$. IPR of scars can be estimated by perturbation theory
Schematic illustration of relevant cat eigenstates in the spectrum	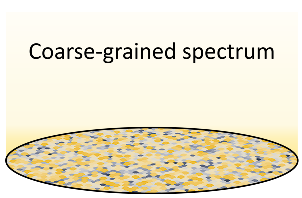	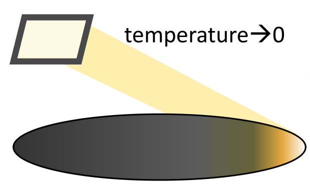	
Examples Parameters: $N = 16$, $\lambda_{1,2}T = 0.05$, $\varphi_1 T = -\pi/2$, $\varphi_2 T = \pi/2 - 0.6$	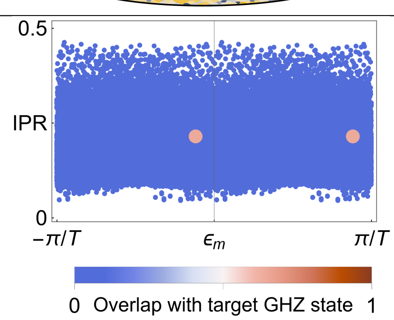	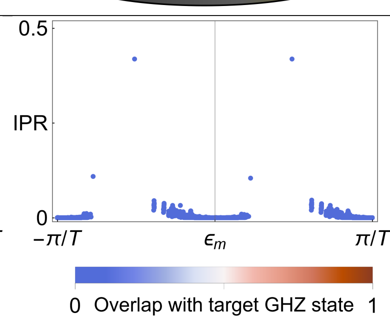	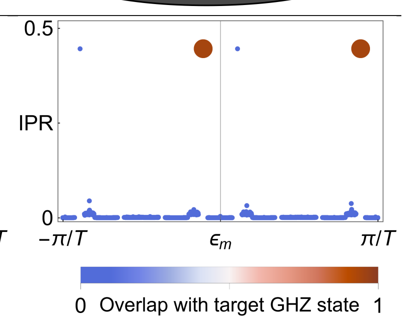
Interaction	$JT = WT = \pi/4$	$J_{jk} = J/\lvert j-k\rvert^{1.5}$, $JT = 0.05$	$JT = 1$
Highest IPR state	Depends on disorder realization	Ferromagnetic pattern	Designed on-demand

Supplementary Table 3. Comparison of features for different mechanisms to engineer cat eigenstates in DTCs using kicked Ising model in Supplementary Eq. (11). In the examples with $N = 16$ qubits, we take a random target GHZ state subspace spanned by $\lvert\boldsymbol{s}\rangle = \lvert 1010010101010000001\rangle$ and $\lvert\bar{\boldsymbol{s}}\rangle = \lvert 0101101010111110\rangle$. The overlap of an eigenstate $\lvert\epsilon_m\rangle$ with GHZ state subspace is computed by $\lvert\langle\epsilon_m\lvert\boldsymbol{s}\rangle\rvert^2 + \lvert\langle\epsilon_m\lvert\bar{\boldsymbol{s}}\rangle\rvert^2$.

$e^{-i\sum_j h_j^z(-\sigma_j^z)}e^{-i\sum_j h_j^z\sigma_j^z}$. Thus, strong disorders in the Ising-even interaction $J_{jk} \in [J-W/2, J+W/2]$ is needed. The resulting spectrum is expected to host extensive numbers of pairwise cat eigenstates, which can show large variation in their IPR values. As an illustration, in the second column of Supplementary Table 3, we choose $JT = JW = \pi/4$ similar to the parameters in Ref. [27], with eigenstate IPRs and quasienergy for a representative disorder sample shown in the bottom row. Cat eigenstates of largest overlap with target GHZ state subspace (specified in the caption) are highlighted by larger dots.

2. **Prethermalization with Landau's symmetry breaking (pLSB).**
In the pLSB Floquet operator $U_F = e^{-iH_{\text{preth}}}e^{-i\pi\sum_j\sigma_j^x/2}$, upon factoring out a global spin flip, remaining terms in H_{preth} satisfy two conditions. First, the interaction J_{jk} is much weaker than driving frequency $J_{jk}T \ll 1$ (high-frequency limit), thereby giving a prethermal time scale $\sim e^{1/J_{jk}T}$ before significant heating occurs. Second, H_{preth} undergoes LSB and induces an ordered ground state. To stabilize the LSB, a one-dimensional system should be long-range interacting. The extended interaction range typically suppresses ground states of inhomogeneous spin patterns akin to magnetic frustration. In the bottom of the third column for Supplementary Table 3, we adopt the interaction $J_{jk} = J/|j-k|^{1.5}$ with exponent ~ 1.5 similar to Ref. [30] for trapped ions. The spectrum of H_{preth} has a small bandwidth compared with Floquet quasienergy window $2\pi/T$ due to high-frequency constraint $JT \ll 1$. This spectrum is duplicated into two pieces by $e^{-i\pi\sum_j\sigma_j^x/2}$. The two cat eigenstates $\sim |\boldsymbol{s}\rangle \pm |\bar{\boldsymbol{s}}\rangle$ of highest IPRs are made of uniform ferromagnetic spin patterns $|\boldsymbol{s}\rangle = |000\ldots\rangle, |\bar{\boldsymbol{s}}\rangle = |111\ldots\rangle$.

3. **Cat scars.**
The cat scars are stabilized by strong Ising interaction $JT \sim 1$. Under this condition, eigenstates are separated to different subspaces according to effective total domain wall numbers. In particular, there are two rare non-ergodic subspaces, each involving only two Fock states. Sign structure in $J_{j,j+1} \equiv J_j$ specifies two pairs of cat scars in these two subspaces, with spin patterns listed below,

$$J_j = (2s_j-1)(2s_{j+1}-1)J \Rightarrow \begin{cases} \frac{1}{\sqrt{2}}(|\bar{s}_1 s_2 \bar{s}_3 s_4 \ldots \bar{s}_{N-1} s_N\rangle + e^{i\gamma'}|s_1 \bar{s}_2 s_3 \bar{s}_4 \ldots s_{N-1}\bar{s}_N\rangle) & \epsilon_+ = E_1 \\ \frac{1}{\sqrt{2}}(|\bar{s}_1 s_2 \bar{s}_3 s_4 \ldots \bar{s}_{N-1} s_N\rangle - e^{i\gamma'}|s_1 \bar{s}_2 s_3 \bar{s}_4 \ldots s_{N-1}\bar{s}_N\rangle) & \epsilon_- = E_1 + \pi \end{cases} \atop \begin{cases} \frac{1}{\sqrt{2}}(|\bar{s}_1 \bar{s}_2 \bar{s}_3 \bar{s}_4 \ldots \bar{s}_{N-1} \bar{s}_N\rangle + e^{i\gamma}|s_1 s_2 s_3 s_4 \ldots s_{N-1} s_N\rangle), & \epsilon_+ = E_2, \\ \frac{1}{\sqrt{2}}(|\bar{s}_1 \bar{s}_2 \bar{s}_3 \bar{s}_4 \ldots \bar{s}_{N-1} \bar{s}_N\rangle - e^{i\gamma}|s_1 s_2 s_3 s_4 \ldots s_{N-1} s_N\rangle) & \epsilon_- = E_2 + \pi \end{cases} \tag{12}$$

where $\bar{s}_j = (1-s_j)$, $E_1 \approx E_{\text{Ising}}(\bar{s}_1 s_2 \ldots \bar{s}_{N-1} s_N), E_2 \approx E_{\text{Ising}}(\bar{s}_1 \bar{s}_2 \ldots \bar{s}_{N-1}\bar{s}_N)$, γ, γ' are constants that can be absorbed into the Fock states as gauge choices. Meanwhile, the scaling of scar IPRs can be obtained order-by-order via Floquet perturbation theory [31], with the dominant order given by

$$\text{IPR} = \frac{1}{2}\frac{1}{(1+\bar{V}^2\lambda^2 N)^2} + O((\lambda^2 N)^2). \tag{13}$$

Here, $\lambda_1 = \lambda_2 = \lambda$ is the perturbation strength, and $\bar{V}^2$ is the coupling constant which can be extracted from numerical data at a single parameter point of a certain λ, N, as will be elaborated later in Supplementary Table 4.

Based on the features of three schemes to engineer cat eigenstates, we next consider their suitability in the practical task of preserving and controlling a targeted GHZ state. This task involves two crucial requirements. First, the scheme should allow for a deterministic selection of the spin patterns for cat eigenstates matching that of the targeted GHZ state. Second, there should be a quantitative control of the quality for relevant cat eigenstates, i.e. in terms of IPR values, so as to effectively protect the GHZ states, especially if the spin patterns for GHZ states are switched during evolution. From these requirements, we see the challenges in exploiting preexisting experimental platforms based on MBL or prethermalization here. MBL DTCs are affluent in the number of cat eigenstates, but the wide range of IPR distribution implies a large variation of the quality for different cat eigenstates. This issue will be discussed further in Supplementary Figures 15 and 16. Also, the prethermal scheme in one dimension chiefly produces uniform (ferromagnetic) spin patterns for cat eigenstates and lacks tunability. In the following, we focus on the cat-scarred DTCs. To lighten notations, we use J_j to denote $J_{j,j+1}$ for both MBL and cat scar cases in the following. Also, we set $T = 1$ to lighten notations below, i.e. $J_jT \to J_j$, although T will be mentioned for bookkeeping driving periods.

B. Properties of cat scar DTCs

In this subsection, we show in more details the essential two properties for cat scars, namely, the capability to engineer different cat scar spin patterns as specified in Supplementary Eq. (12), and the characterization of scar IPRs given in Supplementary Eq. (13).

1. Pattern control

First, we discuss the circuit implementation of cat scar DTCs and demonstrate the method to flexibly switch spin patterns for cat scars. As illustrated in Supplementary Figure 14a, we start from a uniform circuit,

$$U_F = (U3')ZZ(-4)(U3),$$
$$ZZ(-4) = \prod_{j=1}^{N} e^{-4i(\sigma_j^z/2)(\sigma_{j+1}^z/2)}, \qquad U3' = \prod_{j=1}^{N} e^{i\varphi(\sigma_j^z/2)} e^{-i\lambda_2(\sigma_j^y/2)}, \quad U3 = \prod_{j=1}^{N} e^{i\lambda_2(\sigma_j^y/2)} e^{-i\varphi'(\sigma_j^z/2)} e^{-i(\pi-\lambda_1)(\sigma_j^x/2)} \tag{14}$$

Written in the notation $U3(\alpha, \phi, \theta)$ of Supplementary Eq. (4), we have $\alpha = \lambda_2, \phi = \frac{\pi}{2} - \varphi, \theta = -\varphi$ in $U3'$, and $\alpha =$

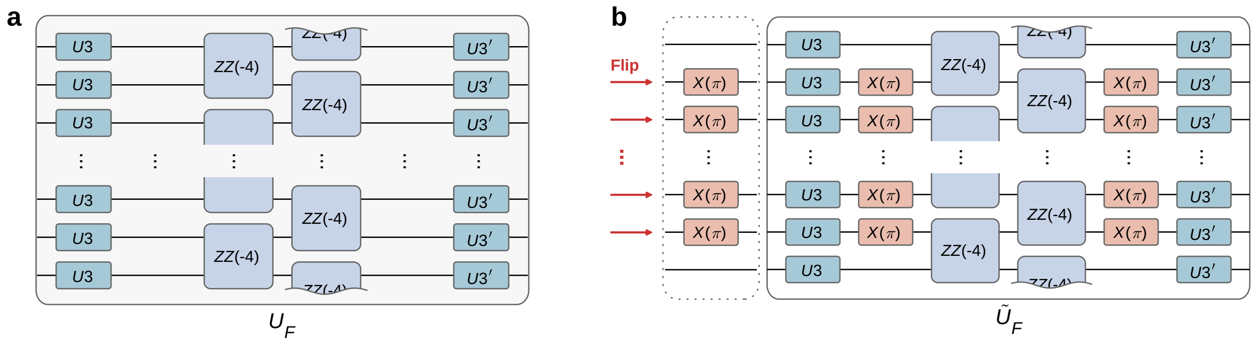

Supplementary Figure 14. Editing the scar patterns by locally changing the sign of Ising interaction, which can be achieved via single-qubit drivings.

$2\arccos\sqrt{\frac{1-\cos\lambda_2\cos\lambda_1-\sin\lambda_2\sin\lambda_1\sin\varphi'}{2}}$, $\phi = -\frac{\pi}{2} - \varphi' + 2\arg\left(1 - ie^{i\varphi'}\cot\frac{\lambda_2}{2}\cot\frac{\lambda_1}{2}\right), \theta = \varphi' - 2\arg\left(1 + ie^{i\varphi'}\tan\frac{\lambda_2}{2}\cot\frac{\lambda_1}{2}\right)$ in $U3$ up to global phases. Note the identities $e^{-i\lambda_2\sigma_j^y/2}\sigma_j^z e^{i\lambda_2\sigma_j^y/2} = \cos(\lambda_2)\sigma_j^z + \sin(\lambda_2)\sigma_j^x$, $e^{-i(\pi/4)\sigma_j^z}\sigma_j^x e^{i(\pi/4)\sigma_j^z} = \sigma_j^y$, and perform a gauge transformation $e^{-i\varphi\sum_{j=1}^N(\sigma_j^z/2)}U_F e^{i\varphi\sum_{j=1}^N(\sigma_j^z/2)}$, we arrive at the physical model

$$U_F = U_2 U_1,$$
$$U_2 = e^{-i\sum_{j=1}^N J\left(\cos(\lambda_2)\sigma_j^z + \sin(\lambda_2)\sigma_j^x\right)\left(\cos(\lambda_2)\sigma_{j+1}^z + \sin(\lambda_2)\sigma_{j+1}^x\right)}$$
$$U_1 = U_P(\varphi_1, \lambda_1, \varphi_2)e^{i\pi\sum_{j=1}^N(\sigma_j^x/2)}, \qquad U_P(\varphi_1, \lambda_1, \varphi_2) = \prod_{j=1}^{N} e^{-i\varphi_1(\sigma_j^z/2)} e^{i\lambda_1(\sigma_j^y/2)} e^{-i\varphi_2(\sigma_j^z/2)}. \tag{15}$$

With a uniform interaction $J_j = J$ here, two pairs of cat eigenstates with ferromagnetic and antiferromagnetic patterns are engineered according to the general relation in Supplementary Eq. (12) (for simplicity, we choose the gauge that extra phase factors are absorbed into the Fock states which is allowed when only one pair of cat eigenstates are involved at a time, and also illustrate the dominant terms for the perturbed cat scars corresponding to their unperturbed anchor point form),

$$\text{Type 1: homogeneous — No extra } X(\pi) \text{ attached}$$
$$\Rightarrow J_j = J \Rightarrow \quad s_1 = s_2 = \cdots = s_N = 1 \quad \Rightarrow \begin{cases} \frac{1}{\sqrt{2}}(|0101\ldots01\rangle + |1010\ldots10\rangle), \\ \frac{1}{\sqrt{2}}(|0101\ldots01\rangle - |1010\ldots10\rangle); \\ \frac{1}{\sqrt{2}}(|0000\ldots00\rangle + |1111\ldots11\rangle), \\ \frac{1}{\sqrt{2}}(|0000\ldots00\rangle - |1111\ldots11\rangle) \end{cases}, \tag{16}$$

where the pair with antiferromagnetic pattern is exemplified in Supplementary Figure 14a and used in our experiment.

To edit the scar spin patterns, we could change the signs of Ising interaction by attaching a pair of $X(\pi)$ gates before and after the $ZZ(-4)$ gates only at certain qubits, as illustrated in Supplementary Figure 14b. That results in a dressed $\tilde{U}_F$. Suppose a pair of $X(\pi)$ gates are attached to Q_j, note $e^{-i\pi\sigma_j^x/2} = -i\sigma_j^x$ and $\sigma_j^x\sigma_j^z\sigma_j^x = -\sigma_j^z$, we can effectively change the sign of J in U_F into a position-dependent one J_j in $\tilde{U}_F$,

$$U_F \sim e^{-iJ[\sigma_j^z\sigma_{j+1}^z]} \quad \rightarrow \quad \tilde{U}_F \sim e^{-i\pi(\sigma_j^x/2)}e^{-iJ[\sigma_j^z\sigma_{j+1}^z]}e^{-i\pi(\sigma_j^x/2)} = -e^{-iJ[(-\sigma_j^z)\sigma_{j+1}^z]} \equiv -e^{-iJ_j[\sigma_j^z\sigma_{j+1}^z]}. \tag{17}$$

Since the signs of J_j depends on both qubits Q_j and Q_{j+1}, generically it is edited into

$$J_j = (2x_j - 1)(2x_{j+1} - 1)J, \tag{18}$$

where $x_j = 1$ denotes no extra $X(\pi)$ gates are attached to Q_j, and $x_j = 0$ means a pair of $X(\pi)$ is attached to Q_j sandwiching the $ZZ(-4)$ gates as in Supplementary Figure 14b. Comparing Supplementary Eq. (18) with Supplementary Eq. (12), we find the identification

$$x_j = s_j, \tag{19}$$

namely, if we want to flip the spin for cat scars with respect to Supplementary Eq. (16) at certain qubits, just sandwich the $ZZ(-4)$ gates at corresponding qubits with pairs of $X(\pi)$ gates. The fact that scar spin patterns can be edited by single-qubit drivings $X(\pi)$ alone means that fast and accurate programming of scars into patterns compatible with GHZ states, which can even be switched during evolution, becomes possible. Also note that because both ferromagnetic and antiferromagnetic scar patterns are achieved simultaneously in Supplementary Eq. (16), at most $N/2$ pairs of $X(\pi)$ are needed to achieve arbitrary patterns. For intuitiveness, we exemplify the results by giving explicitly the gate configurations for the two types of scars in Fig. 4 of the main text,

Type 2: flip 1 at Q_{19} — A pair of $X(\pi)$ gates at Q_{19}

$$\Rightarrow \begin{cases} J_{18} = J_{19} = -J \\ J_{j\neq 18,19} = J \end{cases} \Rightarrow s_{19} = 0, s_{j\neq 19} = 1 \Rightarrow \begin{cases} \frac{1}{\sqrt{2}}(|0101\ldots 01\mathbf{1_{19}}101\ldots 01\rangle + |1010\ldots 10\mathbf{0_{19}}010\ldots 10\rangle), \\ \frac{1}{\sqrt{2}}(|0101\ldots 01\mathbf{1_{19}}101\ldots 01\rangle - |1010\ldots 10\mathbf{0_{19}}010\ldots 10\rangle); \\ \frac{1}{\sqrt{2}}(|0000\ldots 00\mathbf{1_{19}}000\ldots 00\rangle + |1111\ldots 11\mathbf{0_{19}}111\ldots 11\rangle), \\ \frac{1}{\sqrt{2}}(|0000\ldots 00\mathbf{1_{19}}000\ldots 00\rangle - |1111\ldots 11\mathbf{0_{19}}111\ldots 11\rangle). \end{cases} \tag{20}$$

Type 3: maximal deviation — 18 pairs of $X(\pi)$ gates at qubits $Q_{4m+2}, Q_{4m+3}, m = 0, 1, \ldots 8$

$$\Rightarrow \begin{cases} J_{4m+1} = J_{4m+3} = -J \\ J_{4m+2} = J_{4m+4} = J \end{cases} \Rightarrow \quad \boldsymbol{s} = 10011001\ldots 1001 \Rightarrow \begin{cases} \frac{1}{\sqrt{2}}(|0\mathbf{01}10\mathbf{01}1\ldots 0\mathbf{01}1\rangle + |1\mathbf{10}01\mathbf{10}0\ldots 1\mathbf{10}0\rangle), \\ \frac{1}{\sqrt{2}}(|0\mathbf{01}10\mathbf{01}1\ldots 0\mathbf{01}1\rangle - |1\mathbf{10}01\mathbf{10}0\ldots 1\mathbf{10}0\rangle); \\ \frac{1}{\sqrt{2}}(|0\mathbf{11}00\mathbf{11}0\ldots 0\mathbf{11}0\rangle + |1\mathbf{00}11\mathbf{00}1\ldots 1\mathbf{00}1\rangle), \\ \frac{1}{\sqrt{2}}(|0\mathbf{11}00\mathbf{11}0\ldots 0\mathbf{11}0\rangle - |1\mathbf{00}11\mathbf{00}1\ldots 1\mathbf{00}1\rangle). \end{cases} \tag{21}$$

where the highlighted qubits involve pairs of $X(\pi)$ gates.

2. *Quality control*

Preserving a GHZ state of N-qubits imposes stringent and unusual requirements on the DTCs accommodating it. On the one hand, any defective region can bring down the number of qubits being effectively entangled in a GHZ state after several periods of evolution. Meanwhile, a GHZ state made of two Fock state components chiefly overlaps with only two cat eigenstates in the relevant subspace. Thus, compared with properties averaged over all eigenstates, the protective effects on GHZ states depend more sensitively on the quality of a few relevant cat eigenstates. In the following, we numerically and analytically benchmark the scaling of cat scars with the change of system size and perturbation strength. Also, we benchmark the results with MBL DTCs whose properties have been more extensively studied in previous works.

Let us introduce the procedure of scaling analysis more concretely in Supplementary Figure 15. For both cat scar and MBL cases, we fix an arbitrary pair of spin patterns $|\boldsymbol{s}\rangle, |\bar{\boldsymbol{s}}\rangle$ spanning the targeted GHZ state subspace at each system size N, and highlight the IPR for the eigenstate $|\epsilon_m\rangle$ of largest overlap $|\langle \boldsymbol{s}|\epsilon_m\rangle|^2 + |\langle \bar{\boldsymbol{s}}|\epsilon_m\rangle|^2$ with the subspace. For cat scars, we take a single landscape of interaction J_j specified by Supplementary Eq. (12), as illustrated in Supplementary Figure 15a for the same result in Supplementary Table 3. For MBL cases, we fix the same GHZ state subspace as cat scars, and take different disordered sample J_j as exemplified in Supplementary Figure 15b – d. In each sample, we find the eigenstate of largest overlap with the target GHZ state subspace, which are highlighted by red circles. Here for the MBL cases, we can readily see that the IPR of cat eigenstates relevant to a target GHZ state depend sensitively on different disorder realizations. Also, although in each sample there are high IPR eigenstates, there lacks a definitive scheme to ensure that those eigenstates are relevant to a given GHZ state.

In Supplementary Figure 16a – b we show the result of scaling for two system sizes $N = 8$ and $N = 14$. Here we fix the target GHZ state subspace $|s\rangle, |\bar{s}\rangle$ in the caption, and compare the IPRs of relevant cat eigenstates indicated by the largest overlap with GHZ state subspace. The cat scar takes a definite J_j landscape given by Supplementary Eq. (12). To compare with disordered cases more comprehensively, MBL cases take 10^3 samples at each (λ, N) of $J_j \in [J - W/2, J + W/2]$ with $J = W = \pi/4$ as in Supplementary Table 3. From each sample we locate the eigenstate of largest overlap with target GHZ state subspace and form a set of $\mathrm{IPR}_{\mathrm{target}}$ at each (λ, N) contributed by all 10^3 samples. In Supplementary Figure 16a and b, we see that the IPRs of relevant cat eigenstates for MBL cases distribute widely among different samples, signaled by the large separation between highest 10%

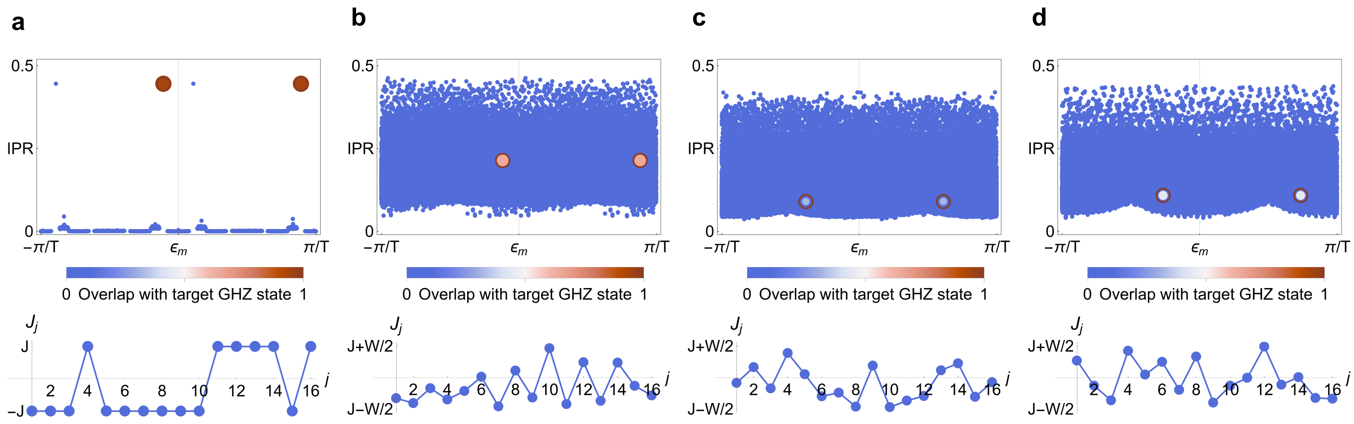

Supplementary Figure 15. Comparison of cat scar and more MBL samples for generating cat eigenstates to accommodate a targeted GHZ state. An arbitrary relevant subspace is spanned by $|\boldsymbol{s}\rangle = |1010010101010000001\rangle$ and $|\bar{\boldsymbol{s}}\rangle = |0101101010111110\rangle$, the same as that in the caption of Supplementary Table 3. Two eigenstates overlapping most strongly with the target GHZ state subspace are highlighted by red circles.

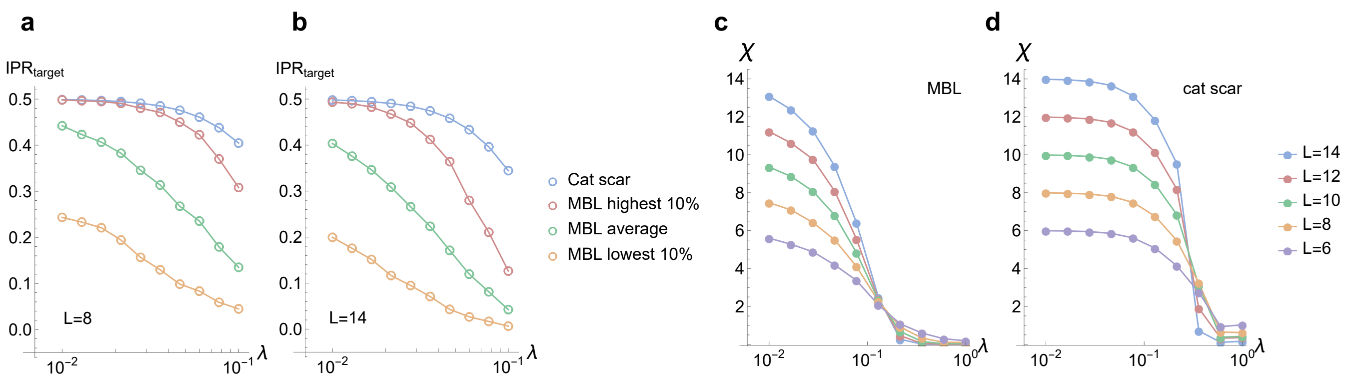

Supplementary Figure 16. Comparison of scaling behaviors for cat scars and MBL cases. **a** and **b**, IPR of the targeted cat eigenstate in cat scar and MBL cases, where we fix $|\boldsymbol{s}\rangle = |10011010\rangle$ for $N = 8$ and $|\boldsymbol{s}\rangle = |01101110001001\rangle$ for $N = 14$. For cat scars, we take a single landscape of interaction specified by Supplementary Eq. (12), and identify the IPR for the eigenstate with largest overlap with $|\boldsymbol{s}\rangle, |\bar{\boldsymbol{s}}\rangle$. For MBL, we take 10^3 samples independently for each (λ, N). In each sample, we pick out the IPR for the cat eigenstate of largest overlap with $|\boldsymbol{s}\rangle, |\bar{\boldsymbol{s}}\rangle$, and form a set of IPR$_{\text{target}}$ contributed by different samples. From the set of IPR$_{\text{target}}$ at each (λ, N), we obtain the average of highest 10% IPRs, lowest 10% IPRs, and overall averaged IPR. **c** and **d**, Edwards-Anderson parameter for estimating stable DTC regimes. In both cases, we average over 10^3 samples at each (λ, N) data point. For MBL, each sample involves a random profile of J_j and we average over all eigenstates. For cat scars, each sample is specified by different target GHZ state subspace $|\boldsymbol{s}\rangle, |\bar{\boldsymbol{s}}\rangle$. We take compatible J_j specified in Supplementary Eq. (12) and the cat scar relevant to the target GHZ subspace.

IPRs and lowest 10% ones. On average the IPRs of cat scars are notably higher than the relevant cat eigenstates in MBL cases, a trend that tends to be enhanced with the increase of system size. Therefore, the data suggests that the cat scar scheme can consistently produce relevant cat eigenstates belonging to those of highest quality in a deterministic way.

Next, we estimate the parameter regimes where cat scars are stable against perturbation. Here we exploit the Edwards-Anderson parameter

$$\chi(\epsilon_m) = \frac{1}{N-1}\sum_{j\neq k}\langle\epsilon_m|\sigma_j^z\sigma_k^z|\epsilon_m\rangle^2, \tag{22}$$

which has been used to benchmark stability of MBL DTCs [32]. A finite value of χ indicates a spatial long-range correlation for the associated eigenstates $|\epsilon_m\rangle$, while for delocalized eigenstates its values approach 0. Note that there are $N(N-1)$ terms in the summation $j \neq k$. For an ideal cat eigenstate, each term contributes 1, giving $\chi = N$ proportional to system size. Thus, χ is an extensive quantity, in contrast to IPR being an intensive one approaching a fixed value $1/2$ for ideal cat eigenstates. Unlike IPRs for measuring the cat eigenstate quality, the usefulness of χ is to give an estimation of transition points between DTC and thermal regimes. In the time-crystalline ordered regime larger system sizes give larger values of $\chi \xrightarrow{\lambda\to 0} N$. Contrarily, in the ergodic limit each term in the summation approaches a value inversely proportional to the Hilbert space size, which decreases exponentially with N, so larger N gives smaller χ. That means the scaling curves will have a crossing point for transitions between the localized DTC regime and the ergodic thermalizing regime with the change of perturbation strength λ. The scaling of $\chi(\epsilon_m)$ is shown in Supplementary Figure 16c and d for MBL and cat scars respectively. In both cases, we take 10^3 samples at each (λ, N) parameter point. For MBL cases, we follow Ref. [32] to select random $J_j \in [\pi/8, 3\pi/8]$ and average over all eigenstates. For the cat scar case, a target GHZ state subspace $|s\rangle, |\bar{s}\rangle$ is randomly selected in each sample. Then, the compatible J_j given in Supplementary Eq. (12) gives the relevant cat scars with associated χ. In both cases we observe the expected crossing point, namely, $\lambda_c \approx 0.129$ for MBL and $\lambda_c \approx 0.36$ for cat scars. Thus, our choice of perturbation strength $\lambda = 0.05$ resides deeply within the DTC regime.

Numerical evidence above has shown qualitatively the cat scar stability and the parameter regimes that can host such robust scars. Experimentally, our system sizes have far transcended the limit for classical computers to perform unbiased simulations (i.e. exact diagonalization) and extract eigenstate properties. As an alternative way to provide quantitative estimations of cat scar quality, we apply IPR predictions by analytical perturbation theory [31] as given in Supplementary Eq. (13).

λ	0.01	0.01292	0.01668	0.02154	0.02783	0.03594	0.04642	**0.05**	0.05995	0.07743	0.1
numerical ($N = 8$)	0.498820	0.4980353	0.496731	0.49457	0.49101	0.4852	0.4758	**0.4721**	0.4609	0.438	0.405
analytical ($N = 8$)	(fit $\bar{V}^2$)	0.4980345	0.496728	0.49456	0.49097	0.4851	0.4755	**0.4717**	0.4601	0.436	0.400
est. err. $(\lambda^2 N)^2$	–	0.000002	0.000005	0.00001	0.00004	0.0001	0.0003	0.0004	0.0008	0.002	0.006
numerical ($N = 14$)	0.497937	0.496566	0.494293	0.490536	0.484367	0.47434	0.45832	**0.45213**	0.4334	0.3963	0.344
analytical ($N = 14$)	0.497938	0.496568	0.494295	0.490537	0.484364	0.47432	0.45826	**0.45205**	0.4332	0.3958	0.343
est. err. $(\lambda^2 N)^2$	0.000002	0.000006	0.00002	0.00004	0.0001	0.0003	0.0009	0.001	0.002	0.007	0.02

Supplementary Table 4. Comparison of analytical (Supplementary Eq. (13)) and numerical results of cat scar IPRs for perturbation strength $\lambda_1 = \lambda_2 \equiv \lambda$ and sizes N.

We first benchmark the accuracy by comparing the analytical results with the numerical data in Supplementary Figure 15a and b for cat scars, as shown in Supplementary Table 4. We extract the coupling strength $\bar{V}^2 = [(2\text{IPR})^{-1/2} - 1]\lambda^{-2}N^{-1} \approx 1.47762$ using a single data point of $\lambda = 0.01, N = 8$, as indicated in the third row and second column of Supplementary Table 4. Then, we can proceed to obtain IPRs for all other (λ, N). In Supplementary Table 4, we see the quantitative agreement between analytical results given by $(1/2)(1 + \bar{V}^2\lambda^2 N)^{-2}$ in Supplementary Eq. (13), and the numerical data corresponding to the cat scar IPRs in Supplementary Figure 16a and b, with differences residing within the estimated errors $(\lambda^2 N)^2$. This error corresponds to the amplitudes of next leading order term in the perturbation series when the most generic perturbations are present. Thus, when considering a specific model, $(\lambda^2 N)^2$ usually overestimates the error and can serve as an upper bound for the errors of analytical predictions.

N	8	10	12	14	16	18	20	**36 (expt.)**
numerical	0.481725	0.47726	0.47284	0.4685	0.4641	0.4598	0.4556	—
analytical	(fit $\bar{V}^2$)	0.47731	0.47296	0.4687	0.4644	0.4603	0.4561	**0.4251**
est. err. $(\lambda^2 N)^2$	—	0.0006	0.0009	0.001	0.002	0.002	0.003	**0.008**

Supplementary Table 5. Numerical and analytical results of the IPRs for cat scars with spin patterns $|0101\ldots01\rangle$, $|1010\ldots10\rangle$, and $\lambda_1 = \lambda_2 = 0.05$. Here parameters are the same as the experimental cases.

Next, we estimate the IPR for experimentally prepared cat scars in a 36-qubit DTC. Here, to access more system sizes, we consider the translation-invariant setup with scars given by Supplementary Eq. (16). This is the major case investigated in the main text. In Supplementary Table 5, we take the experimentally used parameters and vary the system size N where we compare the numerical and analytical results for IPRs of cat scars in the target GHZ state subspace. Again, agreements are found, with errors within the range of next-leading-order strength $(\lambda^2 N)^2$. Based on this, we obtain the IPR of cat scars for the $N = 36$ case in experiment via analytical method as

$$\text{IPR}_{\text{scar}}(N = 36) = 0.4251 \pm 0.008. \tag{23}$$

This value will be used to analyze experimental data for the dynamical macroscopic quantum coherence in Supplementary Note 5 D 1.

C. Macroscopic quantum coherence in static and DTC systems

Our experiments are based on a quantitative characterization of macroscopic coherence for GHZ states. Traditionally, several measurement protocols have been developed to measure the static macroscopic coherence, including parity and multiple-quantum-coherence (MQC) measurements. They both share the similar feature of quantifying the far-off-diagonal elements in the density matrix related to the subspace spanned by the two Fock state components in GHZ states. We would start from the static case, review the essential concepts, and generalize these protocols to the dynamical regime for characterizing unconventional DTC features exhibited by the GHZ states.

We first review how the macroscopic coherence for a static GHZ state is defined and measured. Suppose a target ideal GHZ state of N particles is

$$|\Phi, \boldsymbol{s}\rangle_N = \frac{1}{\sqrt{2}}\left(|\boldsymbol{s}\rangle + e^{-i\Phi}|\bar{\boldsymbol{s}}\rangle\right), \tag{24}$$

with Fock states $|\boldsymbol{s}\rangle = |s_1 s_2 \ldots s_N\rangle$ and $|\bar{\boldsymbol{s}}\rangle = |(1-s_1)(1-s_2)\ldots(1-s_N)\rangle$, $s_j = 1, 0$ as before. If a pure state $|\Psi\rangle$ is generated, the fidelity of such a state compared with the ideal $|\Phi, \boldsymbol{s}\rangle_N$ can be straightforwardly defined as the overlap $\mathcal{F} = |\langle\Psi|\Phi, \boldsymbol{s}\rangle_N|^2 = {}_N\langle\Phi, \boldsymbol{s}|\rho_{\text{expt}}|\Phi, \boldsymbol{s}\rangle_N \in [0, 1]$, where $\rho_{\text{expt}} = |\Psi\rangle\langle\Psi|$, and $\mathcal{F} = 1$ means perfect overlap with highest fidelity. In real experiments, a mixed state represented by a generic density matrix ρ_{expt} can be expanded in the Fock basis, where the subspace relevant to GHZ state patterns are spanned simply a two-by-two matrix

$$\rho_{\text{expt}} = \begin{pmatrix}|\boldsymbol{s}\rangle & |\bar{\boldsymbol{s}}\rangle\end{pmatrix}\begin{pmatrix}P_{\boldsymbol{s}} & a_2 \\ a_2^* & P_{\bar{\boldsymbol{s}}}\end{pmatrix}\begin{pmatrix}\langle\boldsymbol{s}| \\ \langle\bar{\boldsymbol{s}}|\end{pmatrix}. \tag{25}$$

Then, the fidelity of a mixed state ρ_{expt} compared with target GHZ state $|\Phi, \boldsymbol{s}\rangle_N$ can be similarly defined as

$$\mathcal{F} = {}_N\langle\Phi, \boldsymbol{s}|\rho_{\text{expt}}|\Phi, \boldsymbol{s}\rangle_N = \frac{1}{2}\left(P_{\boldsymbol{s}} + P_{\bar{\boldsymbol{s}}}\right) + \text{Re}(a_2 e^{-i\Phi}). \tag{26}$$

Here, real numbers $P_{\boldsymbol{s}}$ and $P_{\bar{\boldsymbol{s}}}$ in diagonal parts of ρ_{expt} represent the probability of observing particle distribution of patterns $|\boldsymbol{s}\rangle$ and $|\bar{\boldsymbol{s}}\rangle$ respectively. Crucially, the off-diagonal element $\text{Re}(a_2 e^{-i\Phi})$ stands for macroscopic coherence of a quantum state, and will be our focus in the following.

First, from the above discussion, it can be understood why $\mathcal{F} > 0.5$ is usually quoted as a benchmark of macroscopic coherence for experimentally generated GHZ states. This is because a density matrix has unit trace $\text{tr}(\rho_{\text{expt}}) = 1$, which means within GHZ subspace $\frac{1}{2}\left(P_{\boldsymbol{s}} + P_{\bar{\boldsymbol{s}}}\right) \leqslant 0.5$ in the first term of Supplementary Eq. (26). For instance, an unentangled Fock state $|1\rangle^{\otimes N}$ gives the density matrix $\rho_{\text{expt}} = |1\rangle^{\otimes N}\,{}^{\otimes N}\langle 1|$, and therefore $P_{\boldsymbol{s}} = 1, a_2 = P_{\bar{\boldsymbol{s}}} = 0$, giving $\mathcal{F} = 0.5$. Thus, the criterion $\mathcal{F} > 0.5$ guarantees $|a_2| \neq 0$, which then verifies macroscopic coherence for a quantum state ρ_{expt}.

Strictly speaking, $\mathcal{F} > 0.5$ is a sufficient but unnecessary condition for the existence of macroscopic coherence $|a_2| \neq 0$ itself, because the diagonal components $\frac{1}{2}\left(P_{\boldsymbol{s}} + P_{\bar{\boldsymbol{s}}}\right)$ of Supplementary Eq. (26) can fairly be smaller than 0.5, implying that a quantum state has partially leaked out from the GHZ pattern subspace, but the remaining components can still exhibit nonzero macroscopic coherence $|a_2| \neq 0$. In conventional experiments, without further aids, usually the coherence a_2 decays much faster than the probability distributions $P_{\boldsymbol{s}}, P_{\bar{\boldsymbol{s}}}$. Namely, usually a_2 quickly decays to zero before probability $\frac{1}{2}\left(P_{\boldsymbol{s}} + P_{\bar{\boldsymbol{s}}}\right)$ notably deviates from 0.5 during dynamical processes, and therefore using $\mathcal{F} > 0.5$ is a good approximation to verify $a_2 \neq 0$ there. However, macroscopic coherence in DTCs can be abnormally robust, as $a_2 \neq 0$ is maintained even when the depolarizing noise (which necessarily causes leakage $\frac{1}{2}\left(P_{\boldsymbol{s}} + P_{\bar{\boldsymbol{s}}}\right) < 0.5$) already plays significant roles. Thus, we opt to observe the off-diagonal elements a_2 of density matrices directly in our experiments, unlike $\mathcal{F}$ contributed by both diagonal and off-diagonal ones.

In the following, we review two widely exploited methods of measuring $|a_2|$ directly, namely, the parity and the multiple-quantum-coherence (MQC) methods. They constitute the conceptual basis for our design of Schrödinger cat interferometry to quantify dynamical macroscopic coherence for evolved GHZ states.

Both methods are built upon the intuition that for a GHZ state of the form in Supplementary Eq. (24), if one applies a phase rotation ϕ on each constituent spin ($\boldsymbol{s} = 0101\ldots$),

$$e^{i\sum_{j=1}^{N}(-1)^j\phi\sigma_j^z/2}|\Phi, \boldsymbol{s}\rangle_N = e^{iN\phi/2}|(\Phi + N\phi), \boldsymbol{s}\rangle_N, \tag{27}$$

the relative phase Φ between two components in Supplementary Eq. (24) is rotated by an enhanced amount proportional to N. Such a phase sensitivity is often exploited to perform ultra-sensitive sensing of external magnetic fields using GHZ states, where a small change in field strength ϕ is amplified by a factor N. This is to be contrasted against other short-range entangled states, i.e. a local product state, where phase rotations on different sites need not purely add up but may cancel each other as large numbers of different Fock states are involved. Thus, the factor N, or equivalently speaking the $\sim 1/N$ periodic response to phase rotation ϕ is a unique character of GHZ states made of two maximally different Fock states.

Following the operation in Supplementary Eq. (27), there are two options to reveal the period-π/N phase rotation response. One option is the **parity** measurement, where the parity operator along, i.e. x-axis, reads

$$\mathcal{P}_x = \prod_{j=1}^{N}\sigma_j^x, \tag{28}$$

It has eigenstates

$$\mathcal{P}_x|\pm,\boldsymbol{s}\rangle_N = \pm|\pm,\boldsymbol{s}\rangle_N, \qquad |\pm,\boldsymbol{s}\rangle_N = \frac{1}{\sqrt{2}}(|\boldsymbol{s}\rangle \pm |\bar{\boldsymbol{s}}\rangle). \tag{29}$$

Correspondingly, an ideal GHZ state can be expressed as

$$|(\Phi+N\phi),\boldsymbol{s}\rangle_N = e^{-i(\Phi+N\phi)/2}\left(\cos\frac{\Phi+N\phi}{2}|+,\boldsymbol{s}\rangle_N + i\sin\frac{\Phi+N\phi}{2}|-,\boldsymbol{s}\rangle_N\right) \tag{30}$$

Thus, the probability of obtaining +1 for the parity measurement is

$$P_{|+,\boldsymbol{s}\rangle} = \cos^2\frac{\Phi+N\phi}{2} = \frac{1}{2}(1+\cos(\Phi+N\phi)). \tag{31}$$

The macroscopic coherence $|a_2|$ can then be read out from the period-$2\pi/N$ oscillation amplitude of $P_{|+,\boldsymbol{s}\rangle}$ with the change of ϕ. In practice, one can combine the phase rotation in Supplementary Eq. (27) and a global spin-flipping exchanging spin x and z basis, namely, $U_{\text{parity}} = e^{i\frac{\pi}{2}\sum_{j=1}^{N}\left(\cos(\phi)\sigma_j^x+\sin(\phi)\sigma_j^y\right)/2}$, $U^{\dagger}_{\text{parity}}\rho_{\text{expt}}U_{\text{parity}}$. Then, the P_{+1} probability for parity corresponds to the probability of observing the ground state $|0\rangle^{\otimes N}$ in the spin-z basis after the operation U_{parity}.

Another option is the **MQC** method more suitable for systems equipped with digital gates. MQC operation involves three consecutive steps, which we illustrate using the ideal GHZ state in Supplementary Eq. (24). First, one similarly performs a phase rotation as in Supplementary Eq. (27), ending up with the GHZ state $|(\Phi+N\phi),\boldsymbol{s}\rangle_N$. Second, different from the parity protocol involving simultaneous spin flips, here one consecutively acts on neighboring qubits with CNOT gates $|11\rangle \leftrightarrow |10\rangle, |01\rangle \leftrightarrow |01\rangle, |00\rangle \leftrightarrow |00\rangle$, which is the inverse of the scheme to generate a GHZ from a product state. Then, the GHZ state is disentangled to

$$|(\Phi+N\phi),\boldsymbol{s}\rangle_N \to \frac{1}{\sqrt{2}}\left(|1\rangle + e^{-i(\Phi+N\phi)}|0\rangle\right)\otimes|0\rangle^{\otimes(N-1)}, \tag{32}$$

namely, the whole phase factor is deposited to the first qubit. Finally, one performs a spin-rotation on the first qubit alone $e^{i\frac{\pi}{4}\sigma_1^x}$, and measure the ground state probability

$$P_{|000...0\rangle} = \cos^2\frac{\Phi+N\phi}{2} = \frac{1}{2}(1+\cos(\Phi+N\phi)), \tag{33}$$

which is of the same character as P_+ in parity measurement. For practical purposes, a spin-flipping π-pulse $\prod_{j=1}^{N}\sigma_j^x$ is usually applied after the generation of GHZ states, before performing the above three steps for MQC measurements. The pulse serves to cancel the dephasing noise accumulated during the GHZ state generation with the corresponding phase noise in MQC measurement processes.

Compared with the static macroscopic coherence measurement, the additional task we need to perform in DTC systems is to reveal the dynamics of coherent phase Φ in GHZ state $|\Phi,\boldsymbol{s}\rangle_N$. In an ideal noise-free setting, one can simply observe the oscillation via, i.e. the traditional MQC measurements $P_{|000...0\rangle} \sim \cos\left[(\Phi+N\phi)(-1)^{t/T}\right]$. However, in practical experiments, the DTC evolution $U_F^{t/T}$ is accompanied by dephasing noise that would endow an additional time-dependent factor $P_{|000...0\rangle} \sim \cos\left[(\Phi+N\phi)(-1)^{t/T} + \Phi_{\text{noise}}(t)\right]$. The dephasing noise contributes a random factor in each cycle, and therefore a definition of the DTC order in terms of the value of the phase factor at a single ϕ is invalid. Importantly, what really serves as the definitive evidence of macroscopic coherence for GHZ state is the $\sim 1/N$ periodicity of the phase response to single-qubit rotation, namely, the $N\phi$ term of the phase factor, rather than the absolute value of Φ that can be redefined via a gauge transformation.

Thus, we define the Schrödinger cat interferometry protocol in the following way, and illustrate its effects on an ideal GHZ state $|\Phi,\boldsymbol{s}\rangle_N$.

1. Generate a GHZ state $|\Phi,\boldsymbol{s}\rangle_N$. Apply phase rotation ϕ on each qubit to levitate the coherent phase for GHZ state into $|(\Phi+N\phi),\boldsymbol{s}\rangle_N$.

2. Evolve with DTC unitary for certain periods, ending up with the state $|(\Phi+N\phi)(-1)^{t/T}+\Phi_{\text{noise}}(t),\boldsymbol{s}\rangle_N$,

3. Apply a spin π-pulse to reduce the effects of dephasing noise, giving $|-(\Phi+N\phi)(-1)^{t/T}-\Phi_{\text{noise}}(t),\boldsymbol{s}\rangle_N$

4. Crucially, perform again single-qubit phase rotation with opposite values $-\phi$, so the GHZ state becomes

$$\left|-N\phi(1+(-1)^{t/T}) - \left(\Phi(-1)^{t/T}+\Phi_{\text{noise}}(t)\right),\boldsymbol{s}\right\rangle_N. \tag{34}$$

5. Apply the reversed circuit for generating GHZ state similar to the last step in MQC measurements, so the ground state probability corresponds to the phase information

$$\mathcal{K}'(\phi, t) \equiv P_{|000...0\rangle} = \cos^2\left[N\phi(1 + (-1)^{t/T}) + \delta\Phi(t)\right] \tag{35}$$

where $\delta\Phi(t) = \Phi(-1)^{t/T} + \Phi_{\text{noise}}(t)$, which does not carry the factor N.

Now, we see that the spatiotemporal structure of cat eigenstates is simultaneously revealed by the first term in the coherent phase factor $-N\phi(1 + (-1)^{t/T})$, without referring to the absolute value of the whole phase factor. Here, the π/N-periodicity in ϕ at even period ends benchmarks the N-qubit macroscopic coherence. Meanwhile, the disappearance and revival of oscillation in ϕ alternating between odd and even periods respectively confirm the period-$2T$ oscillation, and therefore the quasienergy spectral pairing gap π/T for cat scars. To extract the macroscopic coherent part $\sim N\phi$ from the whole phase factor, we perform a Fourier transformation

$$\mathcal{K}'_f(qN, t) = \left|\frac{1}{M}\sum_{k=0}^{M-1} e^{i(qN)\phi(k)}\mathcal{K}'(\phi(k), t)\right|, \qquad \phi(k) = -\frac{\pi}{N} + \frac{2\pi}{NM}k, \quad k = 0, 1, \ldots, (M-1), \tag{36}$$

where M is the number of phase angles ϕ measured in the experiment. Then, the π/N-periodicity in ϕ is reflected by the Fourier component $\mathcal{K}'_f(2N, t) = \mathcal{K}'_f(-2N, t)$. For an ideal GHZ state evolving in an unperturbed DTC where $\mathcal{K}'(\phi, t)$ is given by Supplementary Eq. (35),

$$\mathcal{K}'_f(2N, t) = \frac{1}{4}\frac{1 + (-1)^{t/T}}{2} = \begin{cases} 0.25, & \text{even period } t/T \\ 0, & \text{odd period } t/T \end{cases}. \tag{37}$$

D. Analysis of main text and additional experimental data

1. Phase oscillation of GHZ states

To connect the previous noise-free results with experimental data, we exploit a phenomenological model to simulate the effects of noise. Suppose the error rate on each qubit and over each Floquet driving cycle is e_p. The macroscopic quantum coherence $\mathcal{K}'(\phi, t)$ involves checking simultaneously all qubits, i.e. the ground state probability $P_{|000...0\rangle}$. Thus, $\mathcal{K}'_f(2N, t)$ in an N-qubit system would experience an extra noise-induced decay

$$(1 - e_p)^{Nt}, \qquad e_p = \begin{cases} 0.007, & \text{DTC case with two-qubit gate errors;} \\ 0.003, & \text{Rabi case without two-qubit gate errors} \end{cases}, \tag{38}$$

where the values of e_p are estimated by comparing with experimental data, which are close to the gate error rates.

For cat scar DTCs, the cat scar wave function under perturbation can be written as $\frac{\alpha_0}{\sqrt{2}}(|\boldsymbol{s}\rangle \pm |\bar{\boldsymbol{s}}\rangle) + ...$, where the delocalized fractions have a negligible contribution to IPR, while the dominant part effective for protecting a GHZ state is approximately related to the scar IPR$\approx \alpha_0^4/2$. Therefore, the cat scar IPR is converted to the relevant fraction of the wave function amplitude as $\alpha_0^2 = \sqrt{2}\cdot\sqrt{\text{IPR}} \approx 0.922$, where we use the analytical value $\text{IPR}_{\text{scar}} = 0.4251$ for 36 qubits from Supplementary Table 5. Thus,

$$\frac{\mathcal{K}'_f(2N, t)}{\mathcal{K}'_f(2N, t = 0)} = (1 - e_p)^{Nt} \times (92\%). \tag{39}$$

Thus, the evolution of $\mathcal{K}'_f(2N, t)$ is dominated by a linear-exponential decay caused by noise effect.

For a Rabi oscillator, its evolutions are given by single-qubit rotations,

$$U_F = U_1 = (-i)^N \prod_{j=1}^{N}\left(e^{-i\varphi_1\sigma_j^z/2}e^{i\lambda_1\sigma_j^y/2}e^{-i\varphi_2\sigma_j^z/2}\sigma_j^x\right) \qquad \Rightarrow \qquad U_F^2 \equiv (-1)^N\prod_{j=1}^{N} u_j^2, \qquad u_j = e^{-i(2\alpha)\hat{\boldsymbol{n}}\cdot\boldsymbol{\sigma}_j/2},$$

where the detuning from echoes ($u_j^2 = 1$) for every two periods at each qubit reads

$$\begin{aligned} u_j^2 &= \left(e^{-i\varphi_1\sigma_j^z/2}e^{+i\lambda_1\sigma_j^y/2}e^{-i\varphi_2\sigma_j^z/2}\right)\left(e^{+i\varphi_1\sigma_j^z/2}e^{-i\lambda_1\sigma_j^y/2}e^{+i\varphi_2\sigma_j^z/2}\right) = e^{i\lambda_1(\sigma_j^y\cos\varphi_1 - \sigma_j^x\sin\varphi_1)/2}e^{-i\lambda_1(\sigma_j^y\cos(\varphi_2) - \sigma_j^x\sin(\varphi_2))/2} \\ &= \cos^2\frac{\lambda_1}{2} + \sin^2\frac{\lambda_1}{2}\cos(\varphi_1 - \varphi_2) - i\sin\frac{\lambda_1}{2}\cos\frac{\lambda_1}{2}\left(\sigma_j^x(\sin\varphi_1 - \sin\varphi_2) + \sigma_j^y(-\cos\varphi_1 + \cos\varphi_2)\right) - i\sigma_j^z\sin^2\frac{\lambda_1}{2}\sin(\varphi_1 - \varphi_2). \end{aligned} \tag{40}$$

That gives the detuning angles

$$\alpha = \arccos\left(1 - \sin^2\frac{\lambda_1}{2}(1-\cos(\varphi_1-\varphi_2))\right), \qquad \hat{n}_z = \pm\sin\left[\arctan\left(\tan\frac{\lambda_1}{2}\cos\frac{\varphi_1-\varphi_2}{2}\right)\right], \tag{41}$$

where $\pm$ sign corresponds to $\varphi_1-\varphi_2>0$ or <0. Then, at even periods t/T, we have

$$u_j^{t/T} = e^{-i(\alpha t/T)\hat{\boldsymbol{n}}\cdot\boldsymbol{\sigma}_j/2} = \cos\frac{\alpha t}{2T} - i\sin\frac{\alpha t}{2T}\hat{n}_z\sigma_j^z - i\sin\frac{\alpha t}{2T}(\hat{n}_x\sigma_j^x + \hat{n}_y\sigma_j^y) \tag{42}$$

Acting on a GHZ state, the perturbed Rabi oscillator performs a rotation (at even period ends t/T)

$$\begin{aligned}&\prod_{j=1}^{N} u_j^{t/T}\frac{|s_1s_2\ldots s_N\rangle + e^{i\Phi}|\bar{s}_1\bar{s}_2\ldots\bar{s}_N\rangle}{\sqrt{2}}\\ &= \frac{1}{\sqrt{2}}\left[\left((\cos\frac{\alpha t}{2T} - is_j\sin\frac{\alpha t}{2T}\hat{n}_z)|s_j\rangle + (|\bar{s}_j\rangle\text{ component})\right)^{\otimes N} + e^{i\Phi}\left((\cos\frac{\alpha t}{2T} - is_j\sin\frac{\alpha t}{2T}\hat{n}_z)|\bar{s}_j\rangle + (|s_j\rangle\text{ component})\right)^{\otimes N}\right]\end{aligned} \tag{43}$$

Thus, the probability for the evolved state to stay in the original subspace $|s_j\rangle^{\otimes N}, |\bar{s}_j\rangle^{\otimes N}$ is

$$P_{|s\rangle+\exp(i\Phi)|\bar{s}\rangle} = \left(\cos^2\frac{\alpha t}{2T} + \sin^2\frac{\alpha t}{2T}\hat{n}_z^2\right)^N. \tag{44}$$

Intuitively, we can look at two limits. The strongest perturbation effect is achieved at $\varphi_1-\varphi_2 = \pi \mod 2\pi$, where

$$\begin{aligned}\alpha = \lambda_1, \hat{n}_z^2 = 0 \quad &\Rightarrow P_{|s\rangle+\exp(i\Phi)|\bar{s}\rangle} = \cos^{2N}\frac{\lambda_1 t}{2T} \xrightarrow{N\gg1,\lambda_1 t/2T\ll1} \left(1 - \frac{1}{2!}\frac{\lambda_1^2t^2}{(2T)^2}\right)^{2N}\\ &\approx e^{-N(\lambda_1/2)^2(t/T)^2}\end{aligned} \tag{45}$$

Contrarily, in the limit $\varphi_1-\varphi_2 = 0 \mod 2\pi$, $\alpha = 0 \Rightarrow P_{|s\rangle+\exp(i\Phi)|\bar{s}\rangle} = 1$, a single-spin echo $u_j^2 = 1$ is approached, as can be directly verified by Supplementary Eq. (40). For other values of $\varphi_1-\varphi_2$, we can use the unified form for probability of evolved state to stay in the original GHZ subspace

$$P_{|s\rangle+\exp(i\Phi)|\bar{s}\rangle} \approx e^{-N\lambda_{\text{eff}}^2(t/T)^2}, \qquad \lambda_{\text{eff}}^2 = \left(\frac{\alpha}{2}\right)^2(1-\hat{n}_z^2), \tag{46}$$

where $\alpha, \hat{n}_z$ are given by Supplementary Eq. (41). Several exemplary effective decay rate λ_{eff} and the comparison of expressions for probability in rigorous Supplementary Eq. (46) and the approximated Supplementary Eq. (46) are shown.

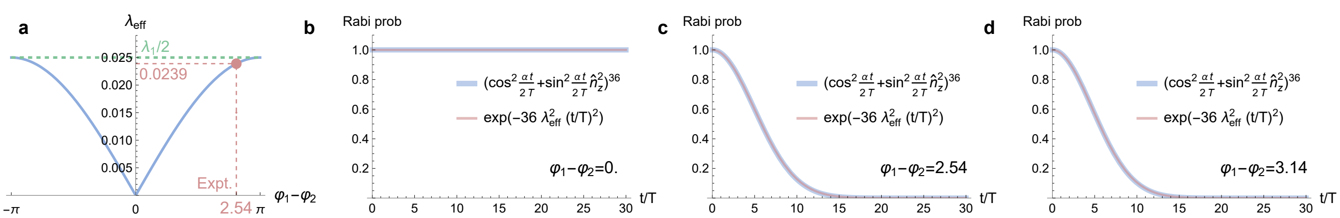

Supplementary Figure 17. **a**, Illustration of the effective decay rate λ_{eff} for macroscopic quantum coherence evolved by Rabi oscillators. The fine-tuned single-spin echo occurs at $\varphi_1-\varphi_2 = 0$, while close to $\varphi_1-\varphi_2 = \pi$ it approaches the maximal value of $\lambda_1/2$. Experimentally we choose a parameter ≈ 2.54 far detuned from the single-spin echo. **b** – **d**, Several examples of probability for a GHZ state to remain in the original Fock subspace as evolved by Rabi oscillators. Experimental situation corresponds to **c**. The agreement between rigorous Supplementary Eq. (44) and the approximated (46) verifies the super-exponential decay.

Based on this result, we obtain the analytical formula for Rabi oscillators

$$\frac{\mathcal{K}_f'(2N,t)}{\mathcal{K}_f'(2N,t=0)} = (1-e_p)^{Nt/T}\times e^{-N\lambda_{\text{eff}}^2(t/T)^2} \tag{47}$$

Crucially, the evolution of macroscopic quantum coherence for Rabi oscillators is dominated by a super-exponential decay $\sim e^{-t^2}$ caused by coherent quantum dynamics taking particles out of the target GHZ state subspace. Supplementary Eq. (47) is to be contrasted against the DTC situation (Supplementary Eq. (39)) with a linear-exponential decay $\sim e^{-t}$ caused simply by external noise. The qualitatively different behaviors lead to sharp distinctions when we plot the evolution of $\mathcal{K}_f'(2N,t)$ in a log-scale figure. As shown in Supplementary Figure 18 (or Fig. 3 in the main text), the DTC case corresponds to a straight line, while the Rabi case shows an accelerated downward-curved decay due to both external perturbation by noise and internal quantum state leakage via coherent quantum dynamics.

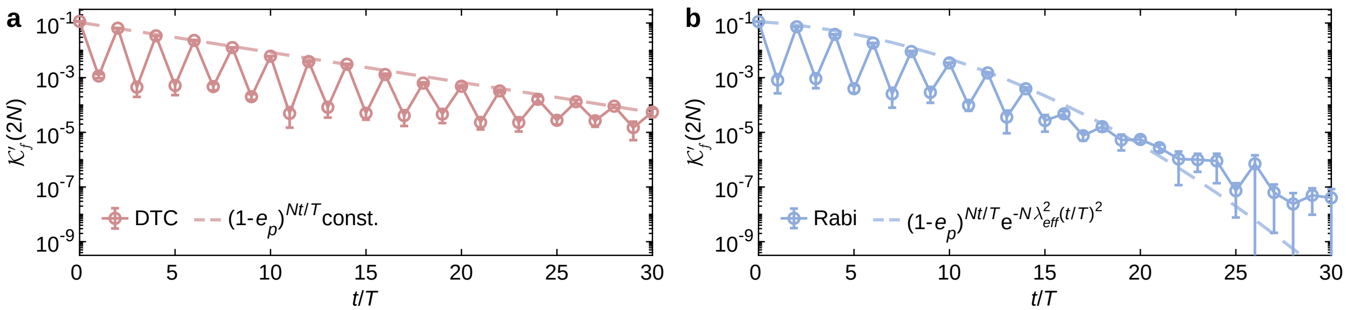

Supplementary Figure 18. A reproduction of Fig. 3 in the main text. **a**, the DTC only experience a linear-exponential decay $\sim e^{-t}$ due to external depolarizing noise, which is represented by a straight line in the log-scale plot. **b**, In contrast, the Rabi oscillator involve a super-exponential decay e^{-t^2} due to the leakage of quantum states from the target GHZ state subspace via internal coherent quantum dynamics. Thus, the Rabi case shows a sharp distinction of being represented by an accelerated downward-curved decay. Here we model the noise effect by the depolarization channel, where DTC experiences a stronger effect $e_p = 0.007$ due to dominant two-qubit gate errors compared with the Rabi case $e_p = 0.003$ with weaker single-qubit errors and environment noise only.

2. *Butterfly velocity for lightcone propagation*

Light cones in a cat scar DTC arise from local thermalization processes under the approximate conservation of total domain wall numbers. Thus, we can derive the butterfly velocity for light cone propagation speed by considering the effects of spin flips by perturbations. Here, large parameters involve Ising interaction J, the spin π pulse, and longitudinal fields φ_1, φ_2. To extract the detuning information that is characterized by small parameters λ_1, λ_2, we consider first the evolution at double-period ends U_F^2 to cancel the perfect spin-flip π-pulse $\exp\left(-i\pi\sigma_j^x/2\right) = -i\sigma_j^x$. Using $\sigma_j^x(\sigma_j^x, \sigma_j^y, \sigma_j^z)\sigma_j^x = (\sigma_j^x, -\sigma_j^y, -\sigma_j^z)$, and perform a gauge transformation $U_F^2 \to e^{i\lambda_2\sum_{j=1}^N \sigma_j^y/2} U_F^2 e^{-i\lambda_2\sum_{j=1}^N \sigma_j^y/2}$ (which amounts to shifting time origin for periodic drivings), we have

$$
\begin{aligned}
U_F^2 = & e^{-iJ\sum_{j=1}^N \sigma_j^z\sigma_{j+1}^z} \times [U_P(0,\lambda_2,0)U_P(\varphi_1,\lambda_1,\varphi_2)e^{-iJ\sum_{j=1}^N(-\sigma_j^z\cos\lambda_2+\sigma_j^x\sin\lambda_2)(-\sigma_{j+1}^z\cos\lambda_2+\sigma_{j+1}^x\sin\lambda_2)}U_p^\dagger(\varphi_1,\lambda_1,\varphi_2)U_P^\dagger(0,\lambda_2,0)] \\
& \times\left[U_P(0,\lambda_2,0)U_P(\varphi_1,\lambda_1,\varphi_2)U_P(-\varphi_1,-\lambda_1,-\varphi_2)U_P^\dagger(0,\lambda_2,0)\right],
\end{aligned} \tag{48}
$$

where $U_P(\varphi_1,\lambda_1,\varphi_2) = \prod_{j=1}^N e^{-i\varphi_1\sigma_j^z/2}e^{i\lambda_1\sigma_j^y/2}e^{-i\varphi_2\sigma_j^z/2}$. Now, we combine the perturbation to two-qubit rotations into

$$
\begin{aligned}
& U_P(0,\lambda_2,0)U_P(\varphi_1,\lambda_1,\varphi_2)\left(\sigma_j^z\cos\lambda_2 - \sigma_j^x\sin\lambda_2\right)U_P^\dagger(\varphi_1,\lambda_1,\varphi_2)U_P^\dagger(0,\lambda_2,0) \equiv \alpha_2\sigma_j^z + \beta_2\sigma_j^x + \gamma_2\sigma_j^y, \\
\alpha_2 &= \cos(\lambda_1)\cos^2(\lambda_2) - \sin(\lambda_1)\sin(\lambda_2)\cos(\lambda_2)[\cos(\varphi_2)+\cos(\varphi_1)] + \sin^2(\lambda_2)[\sin(\varphi_2)\sin(\varphi_1) - \cos(\lambda_1)\cos(\varphi_2)\cos(\varphi_1)], \\
\beta_2 &= \sin(\lambda_2)\cos(\lambda_2)\left[\sin(\varphi_2)\sin(\varphi_1) - \cos(\lambda_1)(1+\cos(\varphi_2)\cos(\varphi_1))\right] - \sin(\lambda_1)\left[\cos^2(\lambda_2)\cos(\varphi_1) - \sin^2(\lambda_2)\cos(\varphi_2)\right], \\
\gamma_2 &= -\left[\sin(\lambda_1)\cos(\lambda_2) + \cos(\lambda_1)\sin(\lambda_2)\cos(\varphi_2)\right]\sin(\varphi_1) - \sin(\lambda_2)\sin(\varphi_2)\cos(\varphi_1).
\end{aligned} \tag{49}
$$

Also, for single-spin perturbations

$$
\begin{aligned}
& U_P(0,\lambda_2,0)U_P(\varphi_1,\lambda_1,\varphi_2)U_P(-\varphi_1,-\lambda_1,-\varphi_2)U_P^\dagger(0,\lambda_2,0) \equiv \prod_{j=1}^N\left(\alpha_0 + i\sigma_j^z\alpha_1 + i\sigma_j^x\beta_1 + i\sigma_j^y\gamma_1\right), \\
\alpha_0 &= \cos^2\frac{\lambda_1}{2} + \sin^2\frac{\lambda_1}{2}\cos(\varphi_2-\varphi_1), \qquad \alpha_1 = \sin^2\frac{\lambda_1}{2}\cos\lambda_2\sin(\varphi_2-\varphi_1) + \sin\frac{\lambda_1}{2}\cos\frac{\lambda_1}{2}\sin\lambda_2(\sin(\varphi_2)-\sin(\varphi_1)) \\
\beta_1 &= -\sin^2\frac{\lambda_1}{2}\sin\lambda_2\sin(\varphi_2-\varphi_1) + \sin\frac{\lambda_1}{2}\cos\frac{\lambda_1}{2}\cos\lambda_2(\sin\varphi_2 - \sin\varphi_1) \\
\gamma_1 &= -\sin\frac{\lambda_1}{2}\cos\frac{\lambda_1}{2}(\cos(\varphi_2)-\cos(\varphi_1))
\end{aligned} \tag{50}
$$

Then, the perturbation effects are grouped into

$$
U_F^2 = \left[e^{-iJ\sum_{j=1}^N \sigma_j^z\sigma_{j+1}^z} e^{-iJ\sum_{j=1}^N(\alpha_2\sigma_j^z+\beta_2\sigma_j^x+\gamma_2\sigma_j^y)(\alpha_2\sigma_{j+1}^z+\beta_2\sigma_{j+1}^x+\gamma_2\sigma_{j+1}^y)}\right]\left[\prod_{j=1}^N(\alpha_0 + i\sigma_j^z\alpha_1 + i\sigma_j^x\beta_1 + i\sigma_j^y\gamma_1)\right], \tag{51}
$$

where β_2, γ_2 characterizing two-spin flips and β_1, γ_1 for single-spin flip are all of perturbative strength $\sim \lambda_1, \lambda_2$.

Up to this point, the derivations are rigorous. To practically extract the butterfly velocity, we make two approximations next. First, we assume the effects of spin flips by perturbations to accumulate independently in different driving cycles and also in the single- and two-qubit drivings separately. This will lead to overestimation of light cone spreading speed at late time because it neglects revivals during coherent quantum dynamics that may delay the thermalization, but would serve as good approximation at early time. Second, based on the eigenstructure of total domain wall separation, we assume that local spin flips during each driving cycle should also conserve the total domain wall numbers.

Based on the first approximation, the one-spin contribution can be estimated by checking the off-diagonal amplitudes $\sim \beta_1, \gamma_1$. Replacing $\sigma_j^x \to 1, \sigma_j^y \to i$ in the second part of Supplementary Eq. (51),

$$v_B^{(1)} = |\beta_1 + i\gamma_1|. \tag{52}$$

For the two-spin terms, we further exploit the approximate conservation of total domain wall numbers. That means we can first replace $P_w \sum_{j=1}^N \sigma_j^z \sigma_{j+1}^z P_w \to (N - 2w)$, where w is the total domain wall number of the initial state, and P_w is a projection to the subspace with w domain walls. Further, domain wall conservation means that a single spin flip can only occur when its two neighboring spins are along opposite directions, namely,

$$\begin{array}{cccl} \uparrow\uparrow\uparrow & \leftrightarrow & \uparrow\downarrow\uparrow & \text{domain wall } 0 \leftrightarrow 2 ✗ \\ \downarrow\uparrow\downarrow & \leftrightarrow & \downarrow\downarrow\downarrow & \text{domain wall } 2 \leftrightarrow 0 ✗ \\ \uparrow\uparrow\downarrow & \leftrightarrow & \uparrow\downarrow\downarrow & \text{domain wall } 1 \leftrightarrow 1 ✓ \\ \downarrow\uparrow\uparrow & \leftrightarrow & \downarrow\downarrow\uparrow & \text{domain wall } 1 \leftrightarrow 1 ✓ \end{array} \tag{53}$$

Such a constraint implies that $P_w \sigma_j^x (\sigma_{j-1}^z + \sigma_{j+1}^z) P_w = 0 = \sigma_j^y (\sigma_{j-1}^z + \sigma_{j+1}^z)$, as σ_{j+1}^z and σ_{j-1}^z take opposite values. Then, the two-spin perturbations are reduced to

$$e^{-iJ\sum_{j=1}^N \sigma_j^z \sigma_{j+1}^z} e^{-iJ\sum_{j=1}^N (\alpha_2\sigma_j^z + \beta_2\sigma_j^x + \gamma_2\sigma_j^y)(\alpha_2\sigma_{j+1}^z + \beta_2\sigma_{j+1}^x + \gamma_2\sigma_{j+1}^y)} \to \text{const.} \times \prod_{j=1}^N e^{-iJ(\beta_2\sigma_j^x + \gamma_2\sigma_j^y)(\beta_2\sigma_{j+1}^x + \gamma_2\sigma_{j+1}^y)}$$
$$= \text{const.} \times \prod_{j=1}^N \left[\cos\left(J(\beta_2^2 + \gamma_2^2)\right) - i \sin\left(J(\beta_2^2 + \gamma_2^2)\right) \times \frac{(\beta_2\sigma_j^x + \gamma_2\sigma_j^y)(\beta_2\sigma_{j+1}^x + \gamma_2\sigma_{j+1}^y)}{\beta_2^2 + \gamma_2^2} \right] \tag{54}$$

Similarly, we consider the off-diagonal amplitude on each site and replace $\sigma_j^x \to 1, \sigma_j^y \to i$, thereby obtaining the contribution from two-spin perturbation

$$v_B^{(2)} = \sin(J(\beta_2^2 + \gamma_2^2)) \tag{55}$$

Altogether, the total butterfly velocity for lightcone propagation from Supplementary Eqs. (50), (49), (52) and (55) reads

$$\begin{aligned} v_B &= v_B^{(1)} + v_B^{(2)}, \\ v_B^{(1)} &= \frac{1}{2} |-(1 - \cos(\lambda_1)) \sin(\lambda_2) \sin(\varphi_2 - \varphi_1) + \sin(\lambda_1)[\cos(\lambda_2)(\sin(\varphi_2) - \sin(\varphi_1)) - i(\cos(\varphi_2) - \cos(\varphi_1)]| \\ v_B^{(2)} &= \sin(J(\beta_2^2 + \gamma_2^2)), \\ \beta_2 &= \sin(\lambda_2)\cos(\lambda_2)\left[\sin(\varphi_2)\sin(\varphi_1) - \cos(\lambda_1)(1 + \cos(\varphi_2)\cos(\varphi_1))\right] - \sin(\lambda_1)\left[\cos^2(\lambda_2)\cos(\varphi_1) - \sin^2(\lambda_2)\cos(\varphi_2)\right], \\ \gamma_2 &= -(\sin(\lambda_1)\cos(\lambda_2) + \cos(\lambda_1)\sin(\lambda_2)\cos(\varphi_2))\sin(\varphi_1) - \sin(\lambda_2)\sin(\varphi_2)\cos(\varphi_1). \end{aligned} \tag{56}$$

Note that when $\lambda_2 = 0$, the single-spin contribution is reduced to $v_B^{(1)} = \frac{1}{2}\sin\lambda_1 |e^{-i\varphi_2} - e^{-i\varphi_1}|$, which has a full-scale single-spin echo condition $\varphi_2 - \varphi_1 = 0 \mod 2\pi$ without light cone propagation. This corresponds to what Supplementary Figure 17a indicates as the effective decay rate λ_{eff} vanishes at the same single-spin echo point. To avoid such a fine-tuned echo and benchmark many-body effects, we experimentally take 10 random samples The deviation from single-spin echo is summarized in Supplementary Table 6. The associated butterfly velocity for the 10 cases are plotted in Supplementary Figure 19a, where numerical simulation of $G_{1j}(t)$ (to be introduced later) for the two cases (samples 1 and 9) close to echoes are shown in Supplementary Figure 19b, c. A very small lightcone is generated here compared with Supplementary Figure 19d for the averaged $G_{1j}(t)$ over all samples.

With the analytical estimation of butterfly velocity in Supplementary Eq. (56), we next compare the results given by experiments and numerical simulations in Supplementary Figure 20. We would chiefly focus on the initial GHZ state with the pattern where one spin (at Q_{10} for numerics or Q_{19} for experiments) is flipped on top of the original antiferromagnetic pattern. The

sample #	1 (~echo)	2	**3 (~expt)**	4	5	6	7	8	9 (~echo)	10
φ_1	1.04943	2.95514	**-1.57008**	0.32882	-0.64870	-0.99062	-0.40049	0.60043	0.92217	1.81469
$\lvert\varphi_1-\varphi_2\rvert$	0.07863	1.98434	**2.54087**	0.64198	1.61950	1.96141	1.37129	0.37037	0.04863	0.84389

Supplementary Table 6. Values of φ_1 for different samples, so as to check whether single-spin echoes ($|\varphi_1 - \varphi_2| = 0 \mod 2\pi$) occur. Here we generate 10 random samples of spatially uniform φ_1 and fix $\varphi_2 = 0.97$. Samples 1 and 9 are close to single-spin echoes, as we can see later in Supplementary Figure 20 that they produce small light cones. To avoid such non-interacting echoes, in most experiments we use $\varphi_1 = -\pi/2$, close to the third sample, which stays far away from single-spin echoes in order to benchmark the interaction effects in stabilizing cat scars against generic perturbation.

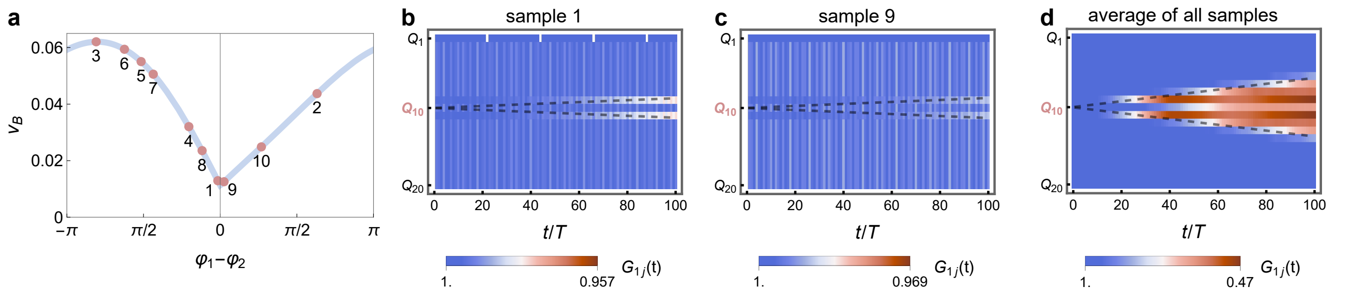

Supplementary Figure 19. **a**, The butterfly velocity given by Supplementary Eq. (56) (blue curve). Red dots corresponds to the 10 samples in Supplementary Table 6. **b**, **c**, Numerical simulation of $G_{1j}(t)$ for the two samples close to single-spin echoes, where we see relatively small light cone and slow thermalization rate. **d**, Numerical simulation of $G_{1j}(t)$ averaged over all 10 samples.

flipped spin generates a mini-ferromagnetic domain of three sites surrounding it, and thermalization would occur starting from the two neighboring spins. Such a spatial structure of thermalization can be revealed by the connected correlation function

$$G_{jk}(t) = \left|\langle\sigma_j^z\sigma_k^z\rangle - \langle\sigma_j^z\rangle\langle\sigma_k^z\rangle\right|. \tag{57}$$

For a noise-free numerical simulation without qubit quality differences, we can choose an "observer" spin, i.e. Q_1, and examine its correlation with other qubits. In the second and fourth columns of Supplementary Figure 20, we plot the value of $G_{1j}(t)$. A qualitative agreement for the shape of lightcone between the analytical prediction of $Q_{10} \pm v_B t$ is observed, with v_B given by Supplementary Eq. (56). In parallel, we compare the analytically derived results with experimental data for each sample in the first and third columns of Supplementary Figure 20. Here, to cancel the error differences in different physical qubits, we opt to check the averaged correlation for each site with all the remaining ones

$$G_j(t) = \frac{1}{N-1}\sum_{k=1\ldots N;k\neq j} G_{jk}(t). \tag{58}$$

Starting from an initial GHZ state where qubit Q_{19} is flipped on top of an overall antiferromagnetic pattern, a lightcone is similarly generated starting from Q_{18}, Q_{20}, with the propagation speed qualitatively in agreement with analytical predictions $Q_{19} \pm v_B t$, with v_B in Supplementary Eq. (56), because thermalization is a local dynamics.

Finally, we present additional experimental data for the light cone propagation as revealed by $G_{jk}(t)$ starting from other initial states or evolved by different $\tilde{U}_F$ in Supplementary Figure 21. Here, to focus on the thermalization ignited by coherent internal quantum dynamics, we take more sweeps over different physical qubits (see caption for details) to cancel the effects of qubit error differences. On the upper left panel, we first show $G_j(t)$ for the initial state with one qubit Q_{19} flipped on top of an antiferromagnetic pattern, but the initial state is evolved by a compatible $\tilde{U}_F$ (in parallel with Fig. 4d in the main text), where we see suppression of lightcone by cat scar DTCs. In contrast, a lightcone spreads out on the upper right panel for the same initial state evolved by the original U_F hosting incompatible antiferromagnetic cat scars. Following this line of investigation, we continue flipping more qubits for the initial states (i.e. 2 for the lower left and 4 for the lower right panels) and evolving each of them under the same U_F with antiferromagnetic cat scars. We indeed see that more sources of thermalization are ignited, each producing a similar light cone until these light cones tend to merge at late time. These results help verify the expectation that the initial GHZ state with qubit pattern 00110011 . . . , where all individual qubits are sources of thermalization (related to Fig. 4e of the main text), undergoes the most rapid thermalization in a cat scar DTC with an incompatible antiferromagnetic cat scars.

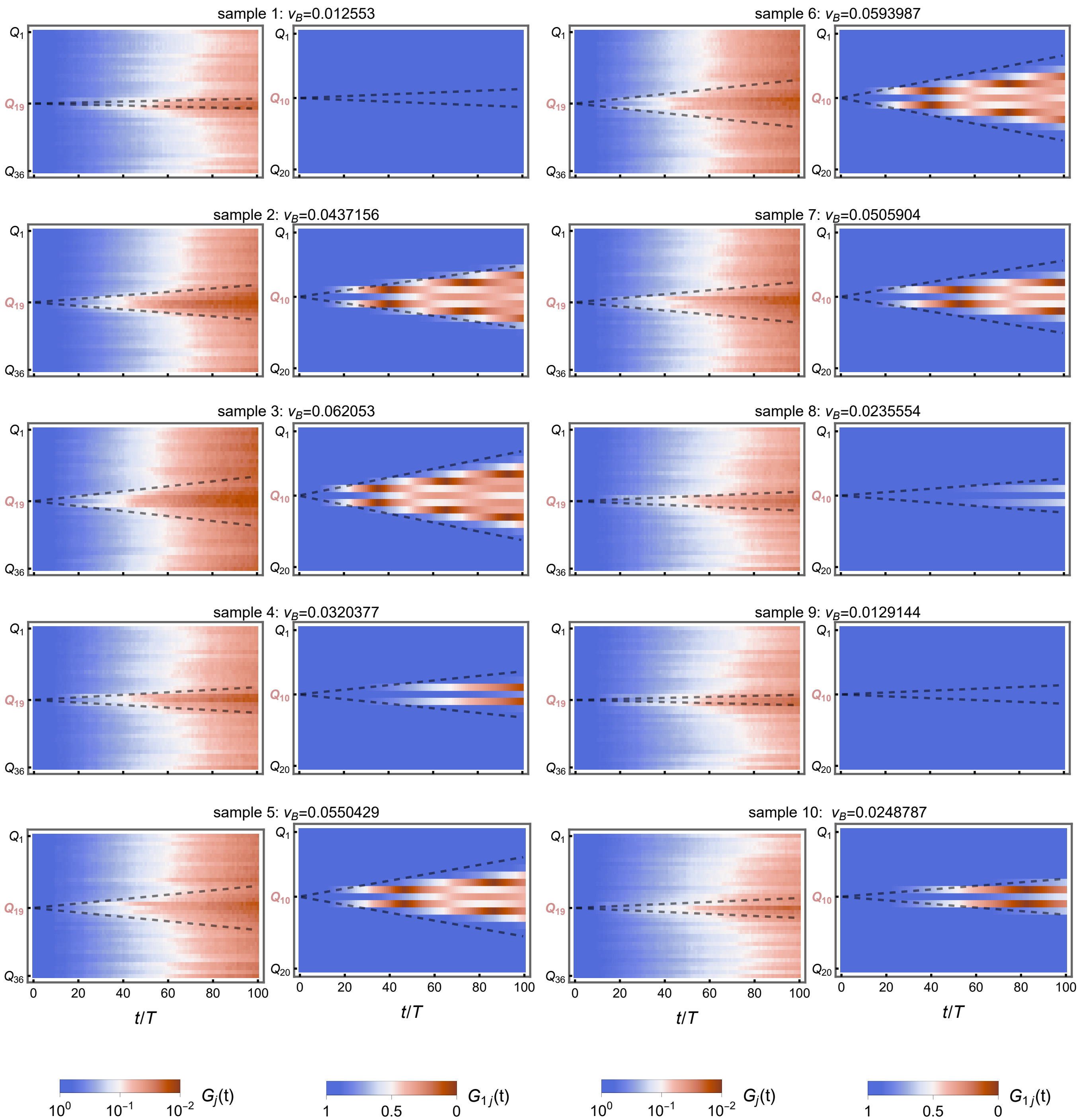

Supplementary Figure 20. (The first and the third columns) Experimentally measured $G_j(t)$ (Supplementary Eq. (58)) for the 10 samples of φ_1 in Supplementary Table 6. Here the initial state is the GHZ state with one qubit (denoted Q_{19}) flipped with respect to an antiferromagnetic pattern, where a thermalizing lightcone stems from the two qubits Q_{18}, Q_{20} centering around flipped Q_{19}. Similar to the main text Fig. 4a, b, and d, we sweep over 6 random physical qubits for the flipped Q_{19}. (The second and the fourth columns) Numerical simulation for $G_{1j}(t)$ where in the noise-free case we choose Q_1 as the observer qubit. The initial state is a GHZ state with one qubit Q_{10} flipped on top of an antiferromagnetic pattern, and similarly lightcones spread out from Q_9, Q_{11} surrounding it. Note that samples 1 and 9 close to single-qubit echoes are further shown in Supplementary Figure 19b and c. In all cases, we compare the thermalizing lightcone with analytical butterfly velocity v_B (dashed lines for $Q_{19} \pm v_B t$ in experimental and $Q_{10} \pm v_B t$ in numerical data) estimated by Supplementary Eq. (56).

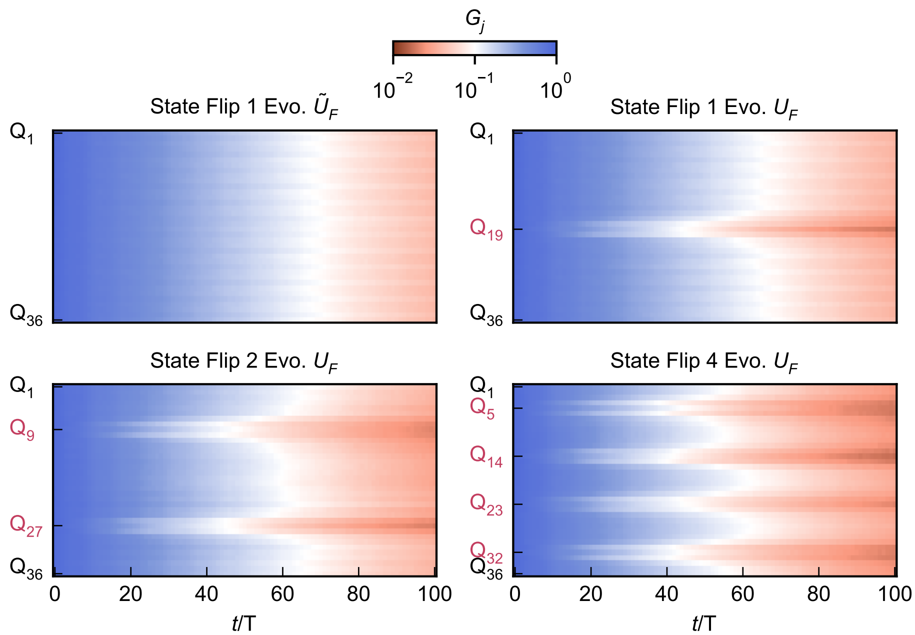

Supplementary Figure 21. $G_j(t)$ **for different initial GHZ states evolving in cat scar DTCs.** Here, for each panel, we take an initial GHZ state, whose qubit pattern involves flipping one (for both of the upper two panels) or more (as denoted by red qubit labels in the lower two panels) qubits on top of an antiferromagnetic pattern. In the upper two panels, the initial state involves Q_{19} flipped on top of an antiferromagnetic GHZ state, which is evolved by a compatible $\tilde{U}_F$ or incompatible (with antiferromagnetic cat scars) U_F respectively. The flipped Q_{19} is swept over 12 equal-spacing physical qubits to cancel qubit error differences. In the lower-left panel, the flipped pair Q_9-Q_{27} are swept over 9 equal-spacing physical qubits. For the Q_5-Q_{14}-Q_{23}-Q_{32} quadruplet on the lower-right panel, we sweep over all physical qubits with 9 possibilities.

3. Comparison with the case of free-decay

In this section, we show the lifetime of GHZ states under free decay, namely, we set all the gates into the same length of idle time and qubits are only influenced by coupling to the environment. Typically, in previous works, one usually compares the lifetime of GHZ states under free decay with that evolved by Rabi driving. The major difference is then caused by the dynamical decoupling of Rabi driving that suppresses correlated dephasing noise (i.e. $\sim \sigma_j^z$ without spin flips). Without π-pulses for dynamical decoupling, the free decay experiences superdecoherence [19] erasing the off-diagonal components of a GHZ state density matrix with an accelerated rate $\sim e^{-N^2 t}$, which is N times faster than the usual $\sim e^{-Nt}$ for depolarization.

In our work, we have included single-spin perturbation to benchmark the robustness of DTCs compared with Rabi oscillators. That affects the overall wave function amplitudes within the Fock subspace related to GHZ states. Thus, to enable sensible comparison with the free-decay case in connection to the previous experiment, we rescale the quantum coherence $\mathcal{K}_f'(2N)$ presented in Fig. 3 of the main text with overall population within the GHZ state subspace represented by all Fourier components $\sum_q \mathcal{K}_f'(q)$, as shown in Supplementary Figure 22. As such, we focus on the *fraction* of the density matrix that retains macroscopic quantum coherence (with period-π/N response to longitudinal fields) relative to the total amplitudes within GHZ subspace.

Supplementary Figure 22 illustrates the comparisons between DTC and the other two cases. We emphasize that in all three cases, we set the same period $T \approx 0.144$ μs. More specifically, for the Rabi driving case where we turn off two-qubit gates, $U_2 = \mathbb{I}$ (identity matrix), we still let the system idle for the same amount of time as that for U_2. In the free-decay case, we set all the gates into idle, $U_F = \mathbb{I}$, and the whole system only experiences uncontrollable interactions among qubits and the external environment. Then, we perform measurement for every $T \approx 0.144$ μs.

We first observe that the "idle" case (green) exhibits the fastest drop of quantum coherence, approaching 0 around $t = 10T$ already. Compared with the DTC case (red) where oscillations persist throughout 30 periods, the fraction of density matrix with macroscopic quantum coherence in the free decay scenario drops approximately three times more quickly.

Further, the Rabi driving case shows a slower drop than the free-decay scenario, but faster than the DTC case starting around $t/T \approx \pi/4\lambda_1 \approx 15$, similar to the result of Fig. 3 in the main text. The late time value 1/30 represents an equal distribution of density matrix in all (totally 30) Fourier components, as coherent dynamics takes the GHZ state into local product state spanning exponentially many ($\sim 2^L$) Fock basis, each incorporates randomized phases and can be driven in or out of the GHZ subspace during dynamics.

The reasons for such differences among DTC, Rabi, and free-decay cases can be more intuitively illustrated by taking several

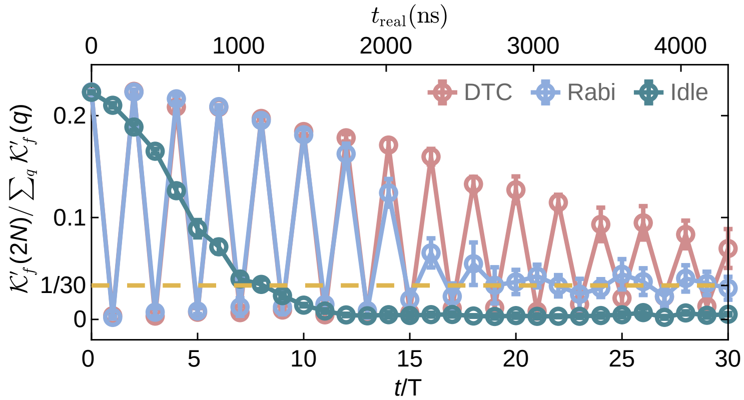

Supplementary Figure 22. Comparison of quantum coherence under different conditions including the free-decay case. Since the idle case does not involve any unitary perturbation, to enable a fair comparison, we rescale the amplitude $\mathcal{K}'_f(2N)$ with overall amplitudes for all components $\sum_q \mathcal{K}'_f(q)$ within the Fock subspace of the target GHZ state.

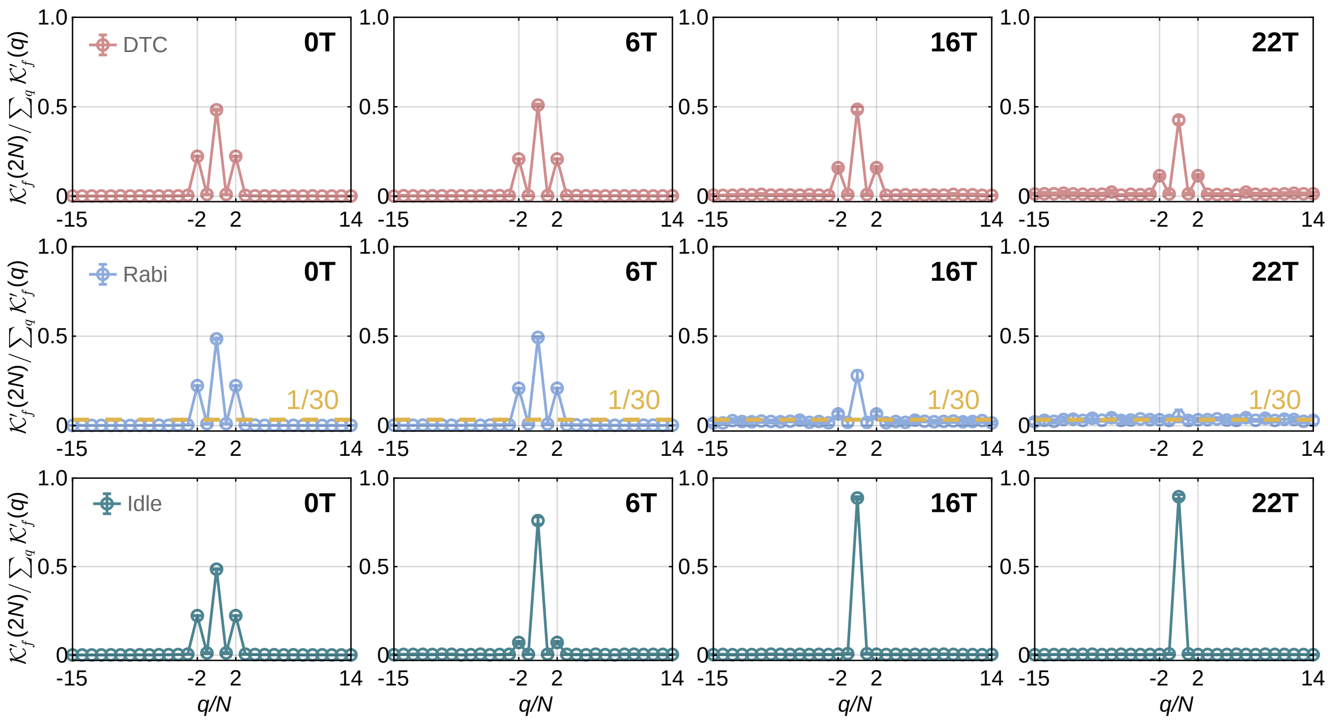

Supplementary Figure 23. Fourier components $\mathcal{K}'_f(q)$ rescaled by the overall amplitudes $\sum_q \mathcal{K}'_f(q)$.

snapshots of all Fourier components, as shown in Supplementary Figure 23. Here, since we rescale the components with the total weight $\sum_q \mathcal{K}'_f(q)$, all the Fourier components q add up to 1, and therefore this figure represents the probability of observing a period-π/qN response of a GHZ state to the longitudinal fields. In particular, the $q = 0$ component represents the diagonal component for the GHZ state density matrix, while the $q = \pm 2N$ components are the N-qubit macroscopic quantum coherence for a GHZ state. We see that the DTC case (red symbols in the first row) witnesses both the diagonal components in the GHZ state subspace and also N-qubit coherence, which persist from the beginning $t = 0T$ to late time $t = 22T$. In contrast, the Rabi driving case (blue symbols in the second row) shows a decay of both $q = 0$ and $q = 2N$ components, arising from the coherent quantum dynamics of imperfect π-pulses taking the wave function out of the GHZ state subspace. The non-interacting unitary dynamics produces a local product state $\sim [\cos(\theta_j)|1\rangle_j + \sin(\theta_j)|0\rangle_j]^{\otimes N}$. These exponentially ($2^N$) many different Fock states respond differently to the longitudinal fields φ_1, φ_2 in U_1, with some of them evolving back to the GHZ state subspace. Thus, we see at late time ($t = 22T$) that all Fourier components possess essentially equal weight 1/30, with 30 being the number of components $q/N = -15, -14, \ldots, 14$. Finally, for the free-decay case (the third row with green symbols), we see that idling gradually erases all components except for the diagonal $q = 0$ one. This is because, without any coherent unitary dynamics, $U_F = \mathbb{I}$, the free-decay by construction exhibits Fock space localization, and therefore maintains the diagonal components. However, the superdecoherence erases any off-diagonal components for the entire density matrix. As such, the longitudinal field cannot affect a classical statistical mixture represented by the density matrix with only diagonal components, and any $q \neq 0$ response vanishes.

E. Generalization to open boundary condition and higher dimensions

While our experiment implements cat scar DTCs in one-dimensional systems with periodic boundary conditions, it is worth emphasizing that neither are necessary and both dimensionality and/or boundary conditions can be generalized. This is straightforwardly demonstrated by the following set of numerical results.

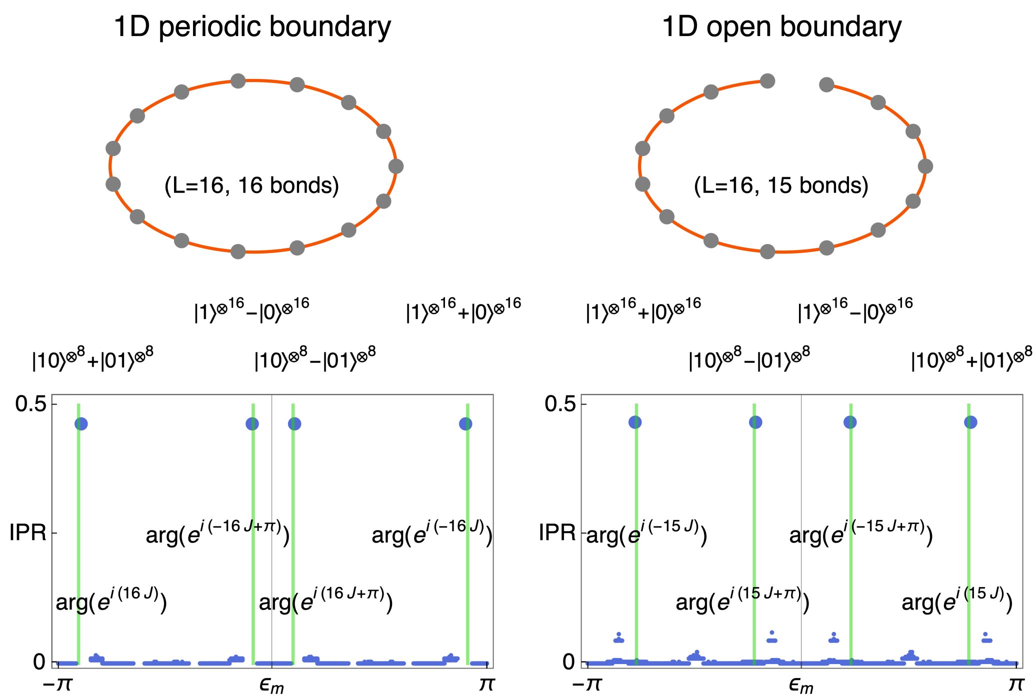

Supplementary Figure 24. Comparison of different boundary conditions in 1D. Changing the boundary condition does not affect the necessary cat scar property, including the high IPR$\sim$ 0.5, predictable scar patterns, and π-quasienergy pairing between scars of the same patterns. The only harmless change is a global quasienergy shift by J for pairwise scars, because the open boundary case has one fewer bond on the edge.

To check different boundary conditions, in Supplementary Figure 24 we perform exact diagonalization to obtain eigenstate IPRs for periodic (left panel) and open (right panel) conditions in 1D for system size $L = 16$. All parameters used here are the same as those in Fig. 3 of our main text. It is readily observed that cat scars exist in both cases, with high IPR$\to$ 0.5 and quasienergy π-pairing between each pair with the same spin pattern. The only minor difference without observable effect is that quasienergy for pairwise cat scars is shifted together by J for open boundary conditions ($\pm 15J$) compared with periodic boundary condition ($\pm 16J$), which is attributable to one fewer bond on the edge if open boundary condition is taken. (Recall that Ising quasienergy contribution $\sim J s_j s_{j+1}$).

A cat scar DTC can also be constructed in higher dimensions straightforwardly, as shown in Supplementary Figure 25 for a 2D example. Here, Ising interactions connect different qubits into a square lattice, and parameter choices are again the same as in Fig. 3 of the main text. As expected, cat scars with two-dimensional ferromagnetic and anti-ferromagnetic patterns show up again with IPR$\sim$ 0.5 and quasienergy π pairing.

Among all dimensions and boundary conditions, we choose to work in a one-dimensional ring experimentally for the following consideration.

1. One-dimensional geometry allows for checking longer-distance correlation and entanglement compared with 2D for a given number of qubits, and therefore provides better benchmarks of all-to-all entangled eigenstates for DTCs.

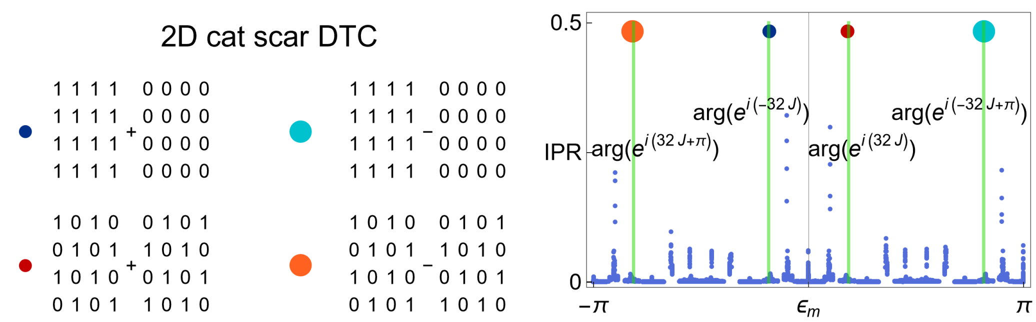

Supplementary Figure 25. Generalization of cat scar DTC models into 2D. We see that the cat scars of 2D FM and AFM patterns show up as expected.

2. Ising model kicked by transverse fields (which can be mapped to driven Kitaev chains without other terms) may give rise to edge Majorana modes if an open boundary is taken [33]. Such edge modes produce Bell-state-like long-range entanglement, which is certainly harmless and even helpful for protecting the GHZ states. But these edge modes only concern two edge spins, not the bulk all-to-all entangled cat eigenstates. Also, Majorana edge states are generated by symmetry-protected topological matters that can be destroyed by symmetry-violating perturbations, unlike DTCs withstanding generic perturbations. Thus, for the purpose of unambiguously showing stable bulk entanglement for DTC eigenstates, it is desirable to avoid edge spins [27, 34]. In our case, we alternatively engineer periodic boundary conditions to erase edge effects entirely, such that any entanglement protection must be provided genuinely by the bulk DTC order without relying on edge modes.

F. Exponential sensitivity of GHZ states in benchmarking spectral-paired cat eigenstates

Over the past decade, DTCs have been probed in many experiments, which usually evolve a local product state and measure the few-body observables, such as one-body magnetic orders and two-body correlation functions. In contrast, we resort to a globally entangled GHZ state which allows for measuring the N-body observable, the macroscopic quantum coherence $\mathcal{K}'_f(2N, t)$. We will illustrate in this section the distinctions between the two types of probe by local product states versus the GHZ states in benchmarking the long-sought feature of DTCs: the spectral-paired cat eigenstates with all-to-all entanglement.

DTC is widely known for its hallmark signature of period-doubled oscillation of local magnetic order, which represents a spontaneous breaking of time translation symmetry. While period-doubled oscillations with certain stability may exist in many scenarios, dating back to the Faraday wave several centuries ago [34, 35], one unique feature for a DTC, which was pointed out since the original sets of studies in 2016 (i.e. Ref. [36]), is that *the lifetime of local spin oscillation prolongs exponentially with system size N*. From the viewpoint of local dynamics, this is surprising: it means that even if we fix the local parameters around a spin at j_0 unchanged, and only add a few spins at sites far away, the lifetime of oscillation at j_0 would increase by several orders of magnitude. This is to be contrasted with our usual expectation that such far-away spins can at most induce some late-time fluctuations.

For illustrations, we model the two scenarios in Supplementary Figure 26. The long-range-entangled case for a certain site j_0 corresponds to the cat scar DTC presented in our main text, where we see that adding a few more spins to the system, while keeping all local parameters unchanged, increases the *local* oscillation at j_0 by orders of magnitudes (i.e. from $\sim 10^6 T$ for $N = 8$ to $\sim 10^{10} T$ for $N = 12$). This is to be contrasted against the short-range-entangled case. Here, we generalize the main text model by setting all Ising bonds $J_{|j-j_0|>2} = 0.1$ and setting strong local perturbation $\lambda_1 = 1.28$ for the distant sites $|j - j_0| > 2$. Then, the site j_0 becomes short-range-entangled with only the neighboring 2 sites. In this case, we see that adding more spins at the disentangled regions essentially does not affect the local oscillation at j_0, as the system sizes $N = 8, 10, 12$ all give the similar $\sim 10^4$ oscillation periods.

The reason for the exponential lifetime scaling of DTCs lies exactly at the long-range-entanglement of the underlying eigenstates, namely, the eigenstates are GHZ-like cat eigenstates. This way, any single spin "knows" how large the system is, as quantified by the mutual information [36, 37] among distant spins. Such globally entangled cat eigenstate pair gives rise to the unique physics of spectral pairing: Under generic perturbation, the quasienergy for a pair of cat eigenstates can only shift together by the same amount, but their quasienergy *difference* is fixed to be π up to exponential accuracy $O(e^{-N})$ [31, 38], corresponding to exponentially long lifetime. However, although such exponential scaling has been seen in lots of numerical works, it is unpractical for any experiment to access the exponentially late time of $10^{6\sim12}$ periods. In other words, based on few-body probes for evolved local product states, it is extremely challenging to distinguish the long-range and short-range entangled eigenstates underlying the subharmonic oscillations, as illustrated in the lower panels of Supplementary Figure 26. Thus, it remains

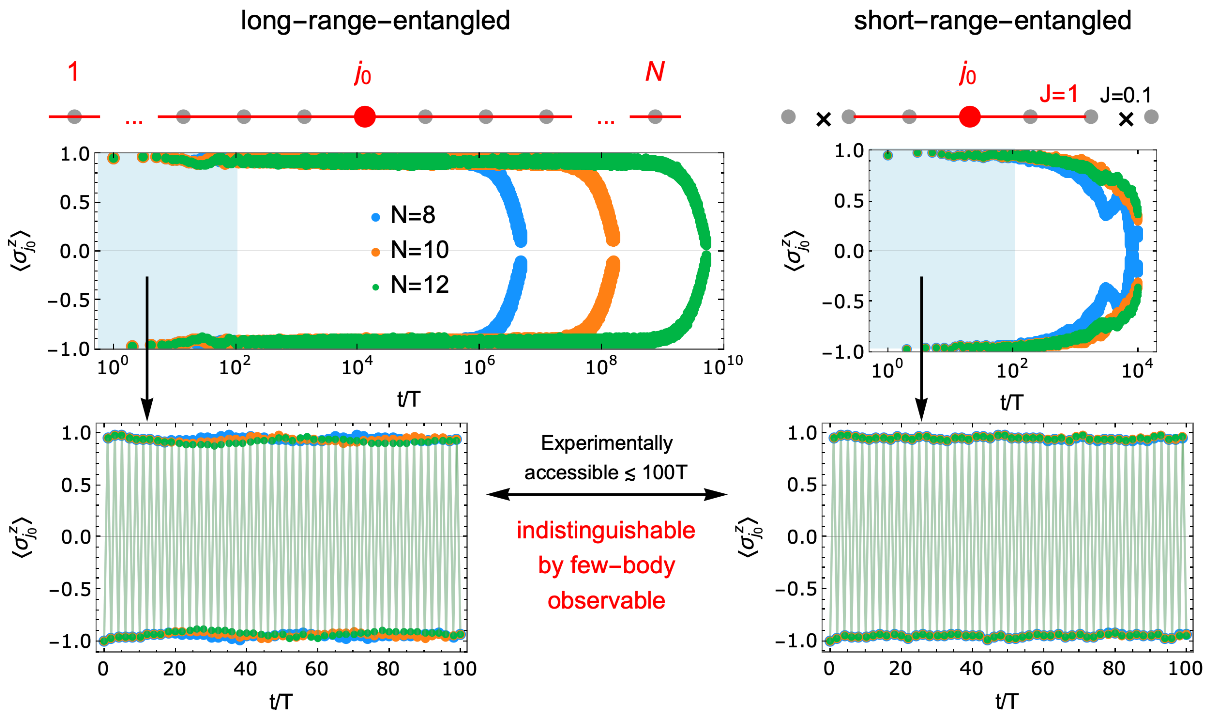

Supplementary Figure 26. Challenge to prove long-range-entangled cat eigenstates in a DTC using conventional few-body observables. (Top left) A long-range entangled DTC in our case with pairwise cat eigenstates gives rise to exponentially long lifetime $\sim e^N$ for the oscillation of $\langle\sigma_j^z\rangle$. (Top right) In contrast, short-range-entangled systems exhibit dynamics dictated by local physics with little relevance to global system size. (Bottom panels) However, experiments across various platforms can only access early time, so it is hard to benchmark the cat eigenstates using local probes unambiguously. Here the long-range-entangled case is numerically simulated using the main text model, where all parameters are the same as in Fig. 3 of the main text except for larger $\lambda_1 = 0.25 < \lambda_c = 0.36$ to observe DTC decay. The short-range-entangled one is further modeled by tuning Ising interaction $J = 0.1$ and perturbation $\lambda_1 = 1.28$ for sites $|j - j_0| \geqslant 3$, such that j_0 is fully disentangled from the system 3 sites away. Initial states are all local product states $|1010\dots\rangle$.

a long-sought goal to find definitive experimental evidence for the pairwise cat eigenstates, which nails down the existence of long-range-entangled DTCs.

From the above discussion, we identify the crucial *physical objective in the experiment: accurately determining whether all spins are entangled in the eigenstates*. Only when all N spins are entangled would a system yield the characteristic DTC lifetime $\sim e^N$. Otherwise, the system could be decomposed into several mutually disentangled regions, and increasing N cannot extend the oscillation lifetime exponentially. Correspondingly, let us compare the effectiveness of two methods for such purposes, namely, the conventional few-body probe (i.e. local magnetic order) associated with local product states, and the N-body probe we adopt for the GHZ state.

In Supplementary Figure 27, we show the numerical results where we use two methods to benchmark the same model U_F, in which a controllable number of spins are disentangled. Specifically, we start from our main text model with parameters the same as those in Fig. 3 there, such that all N qubits are entangled in the cat scar eigenstates. Then, we controllably disentangled 1, 2, or 3 spins from the bulk, and see how sensitive the two methods can detect such defective spins. This is achieved by setting the two bonds connecting the disentangled site with weak interaction $J = 0.1$, and endowing large perturbation λ_1 at the disentangled site. In practice, such disentangled spins can be caused by external circuit or qubit quality differences, or internal parameter differences if disorders exist. Thus, for each of the $N_{\rm d} = 1, 2, 3$ case in Supplementary Figure 27, we take sample average over 100 samples with random locations and random $\lambda_1 \in [0.8, 1.2]$ for disentangled spins, in order to extract universal behaviors independent of accidental microscopic details. Qualitatively different behaviors then emerge between the two methods in Supplementary Figure 27.

1. Few-body observable for local product states (left panel in Supplementary Figure 27). Here, we start with the product state $|1010\dots\rangle$ of antiferromagnetic pattern, and calculate the autocorrelator $C(t) = (1/L)\sum_j\langle\sigma_j^z(t)\sigma_j^z(0)\rangle$, which is a widely used quantity in previous experiment and numerics. Without disentangled qubits $N_{\rm d} = 0$ (blue), we observe an expected period-2T oscillation between $C(t) \sim (-1)^{t/T}$. Then, we see that disentangling each qubit, in the first 100 periods relevant to experiments, only causes a additive decrease of oscillation amplitude by $(1/N)$, which vanishes for larger system sizes.

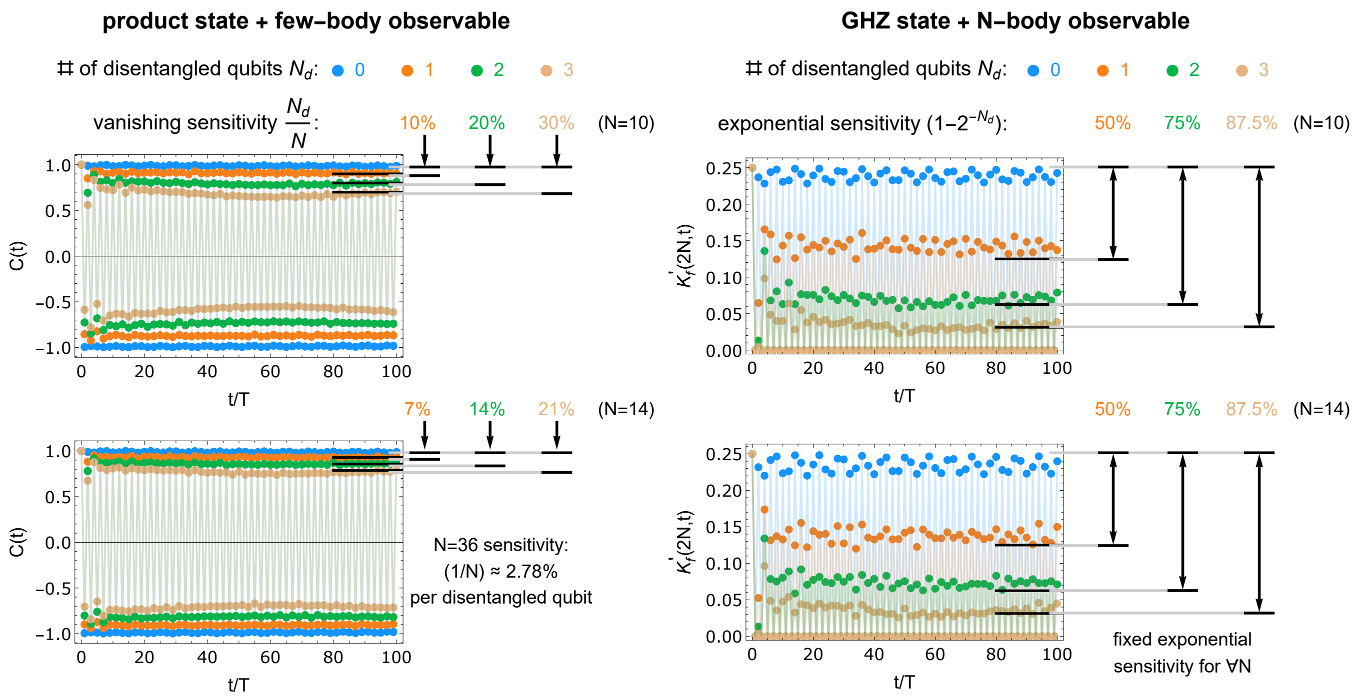

Supplementary Figure 27. Comparison of sensitivity in probing N-qubit entangled cat eigenstates using two methods. Here, we use the same model U_F in both cases, where we start from the main text model with the same parameters as in Fig. 3 of the main text. Then, we disentangle a certain qubit (i.e. at site k) by *locally* weakening its two neighboring Ising bonds $J_{k-1} = J_k = 0.1$ and enhancing the perturbation at site k to $\lambda_1 \in [0.8, 1.2]$, while parameters elsewhere are unchanged. This way, we can controllably disentangle N_d qubits from the system. To extract generic behaviors independent of microscopic details, for each case of $N_\mathrm{d} = 1, 2$, or 3, we average over 100 samples with random locations and random local $\lambda_1 \in [0.8, 1.2]$ for the disentangled qubits. In the left panel, initial states are local product states $|101010\ldots\rangle$, and we numerically evaluate the normalized autocorrelators $C(t) = (1/L)\sum_j \langle \sigma_j^z(t)\sigma_j^z(0)\rangle$. We see that each disentangled qubit invokes a minor change $(1/N)$, approaching 0 for large system sizes N. In the right panel, initial states are instead GHZ states $(|1010\ldots\rangle + |0101\ldots\rangle)/\sqrt{2}$, and we calculate the macroscopic quantum coherence $\mathcal{K}_f'(2N, t)$ as in the main text. We see a fixed exponential accuracy as N_d disentangled qubit suppresses the oscillation amplitude to $1/2^{N_\mathrm{d}}$, independent of system size N.

For instance, in our $N = 36$ qubits system, one disentangled qubit will only incur an amplitude drop by $(1/N) \approx 2.78\%$, a vanishingly small quantity that can fairly be washed out by fluctuations. That means decomposing the N qubits into several mutually disentangled regions is hardly noticeable by the local probe.

2. N-body observable for GHZ states (right panel in Supplementary Figure 27). Sharp contrasts are revealed if we start from a GHZ state $(|1010\ldots\rangle + |0101\ldots\rangle)/\sqrt{2}$, and calculate the macroscopic quantum coherence $\mathcal{K}_f'(2N, t)$ as in Fig. 3 of the main text. Without disentangled qubits ($N_\mathrm{d} = 0$), as in our main text, the oscillation amplitudes of $\mathcal{K}_f(2N, t)$ approach the value $1/4$, which represents an ideally protected GHZ state [see Eq. (S36)]. Then, each disentangled qubit suppresses the oscillation amplitude by a factor of $1/2$, leading to the *exponential suppression* $1/2^{N_d}$ *if* N_d *qubits are disentangled*. Contrary to the few-body probe $C(t)$ that has shrinking sensitivity for larger systems, the N-body observable $\mathcal{K}_f'(2N, t)$ here has a fixed exponential sensitivity regardless of system size. Thus, the observation in Fig. 3 of our main text, with oscillation amplitudes predicted by an analytical theory for cat scar DTCs, offers strong evidence of a globally entangled cat eigenstate pair, because just a few defective spins can bring down the amplitude by orders of magnitude.

Such a contrast is a reflection that few-body observables are only affected by local parameters, but the GHZ state with N-body observable would sensitively detect whether *all* spins are *simultaneously* in the GHZ state subspace with macroscopic quantum coherence. Then, in the latter case, each disentangled spin would take random directions, with $1/2$ probability of remaining in the original direction. Due to probability multiplication, N_d disentangled spins would lead to a suppression of amplitude to $1/2^{N_\mathrm{d}}$. In applications, the extreme sensitivity of GHZ state has often been exploited, which usually only concerns the amplified *phase* angle as single-qubit phase rotations $e^{i\phi\sigma_j^z}$ will accumulate into a large relative phase $e^{iN\phi}$ between the two components in a GHZ state. Our discussion above, instead, illustrates a more generic sensitivity of GHZ states to arbitrary spin rotations, where any defective spin would be revealed by the amplified exponential amplitude suppression.

In summary, observing GHZ states in a DTC offers a unique and accurate benchmark of N-qubit entangled cat eigenstate pair, which is the defining theoretical feature long sought after for DTCs. The amplitude of $\mathcal{K}_f'(2N,t)$ matching that predicted by defect-free analytical theory constitutes strong evidence that the underlying cat eigenstate pair is genuinely N-qubit entangled, as any disentangled qubits will suppress this amplitude exponentially. The temporal period-$2T$ oscillation of $\mathcal{K}_f'(2N,t)$ further proves the quasienergy spectral difference π, accomplishing the direct experimental proof of spectral-paired cat eigenstates robust against generic perturbations.

---

[1] S. Xu, Z.-Z. Sun, K. Wang, L. Xiang, Z. Bao, Z. Zhu, F. Shen, Z. Song, P. Zhang, W. Ren, X. Zhang, H. Dong, J. Deng, J. Chen, Y. Wu, Z. Tan, Y. Gao, F. Jin, X. Zhu, C. Zhang, N. Wang, Y. Zou, J. Zhong, A. Zhang, W. Li, W. Jiang, L.-W. Yu, Y. Yao, Z. Wang, H. Li, Q. Guo, C. Song, H. Wang, and D.-L. Deng, Digital Simulation of Projective Non-Abelian Anyons with 68 Superconducting Qubits, Chinese Phys. Lett. **40**, 060301 (2023).

[2] Y. Yao, L. Xiang, Z. Guo, Z. Bao, Y.-F. Yang, Z. Song, H. Shi, X. Zhu, F. Jin, J. Chen, S. Xu, Z. Zhu, F. Shen, N. Wang, C. Zhang, Y. Wu, Y. Zou, P. Zhang, H. Li, Z. Wang, C. Song, C. Cheng, R. Mondaini, H. Wang, J. Q. You, S.-Y. Zhu, L. Ying, and Q. Guo, Observation of many-body Fock space dynamics in two dimensions, Nat. Phys. **19**, 1459 (2023).

[3] S. Boixo, S. V. Isakov, V. N. Smelyanskiy, R. Babbush, N. Ding, Z. Jiang, M. J. Bremner, J. M. Martinis, and H. Neven, Characterizing quantum supremacy in near-term devices, Nat. Phys. **14**, 595 (2018).

[4] F. Arute, K. Arya, R. Babbush, D. Bacon, J. C. Bardin, R. Barends, R. Biswas, S. Boixo, F. G. S. L. Brandao, D. A. Buell, B. Burkett, Y. Chen, Z. Chen, B. Chiaro, R. Collins, W. Courtney, A. Dunsworth, E. Farhi, B. Foxen, A. Fowler, C. Gidney, M. Giustina, R. Graff, K. Guerin, S. Habegger, M. P. Harrigan, M. J. Hartmann, A. Ho, M. Hoffmann, T. Huang, T. S. Humble, S. V. Isakov, E. Jeffrey, Z. Jiang, D. Kafri, K. Kechedzhi, J. Kelly, P. V. Klimov, S. Knysh, A. Korotkov, F. Kostritsa, D. Landhuis, M. Lindmark, E. Lucero, D. Lyakh, S. Mandrà, J. R. McClean, M. McEwen, A. Megrant, X. Mi, K. Michielsen, M. Mohseni, J. Mutus, O. Naaman, M. Neeley, C. Neill, M. Y. Niu, E. Ostby, A. Petukhov, J. C. Platt, C. Quintana, E. G. Rieffel, P. Roushan, N. C. Rubin, D. Sank, K. J. Satzinger, V. Smelyanskiy, K. J. Sung, M. D. Trevithick, A. Vainsencher, B. Villalonga, T. White, Z. J. Yao, P. Yeh, A. Zalcman, H. Neven, and J. M. Martinis, Quantum supremacy using a programmable superconducting processor, Nature **574**, 505 (2019).

[5] I. Buluta and F. Nori, Quantum Simulators, Science **326**, 108 (2009).

[6] E. Knill, Quantum computing with realistically noisy devices, Nature **434**, 39 (2005).

[7] A. Omran, H. Levine, A. Keesling, G. Semeghini, T. T. Wang, S. Ebadi, H. Bernien, A. S. Zibrov, H. Pichler, S. Choi, J. Cui, M. Rossignolo, P. Rembold, S. Montangero, T. Calarco, M. Endres, M. Greiner, V. Vuletić, and M. D. Lukin, Generation and manipulation of Schrödinger cat states in Rydberg atom arrays, Science **365**, 570 (2019).

[8] I. Pogorelov, T. Feldker, C. D. Marciniak, L. Postler, G. Jacob, O. Krieglsteiner, V. Podlesnic, M. Meth, V. Negnevitsky, M. Stadler, B. Höfer, C. Wächter, K. Lakhmanskiy, R. Blatt, P. Schindler, and T. Monz, Compact ion-trap quantum computing demonstrator, PRX Quantum **2**, 020343 (2021).

[9] S. A. Moses, C. H. Baldwin, M. S. Allman, R. Ancona, L. Ascarrunz, C. Barnes, J. Bartolotta, B. Bjork, P. Blanchard, M. Bohn, J. G. Bohnet, N. C. Brown, N. Q. Burdick, W. C. Burton, S. L. Campbell, J. P. Campora, C. Carron, J. Chambers, J. W. Chan, Y. H. Chen, A. Chernoguzov, E. Chertkov, J. Colina, J. P. Curtis, R. Daniel, M. DeCross, D. Deen, C. Delaney, J. M. Dreiling, C. T. Ertsgaard, J. Esposito, B. Estey, M. Fabrikant, C. Figgatt, C. Foltz, M. Foss-Feig, D. Francois, J. P. Gaebler, T. M. Gatterman, C. N. Gilbreth, J. Giles, E. Glynn, A. Hall, A. M. Hankin, A. Hansen, D. Hayes, B. Higashi, I. M. Hoffman, B. Horning, J. J. Hout, R. Jacobs, J. Johansen, L. Jones, J. Karcz, T. Klein, P. Lauria, P. Lee, D. Liefer, S. T. Lu, D. Lucchetti, C. Lytle, A. Malm, M. Matheny, B. Mathewson, K. Mayer, D. B. Miller, M. Mills, B. Neyenhuis, L. Nugent, S. Olson, J. Parks, G. N. Price, Z. Price, M. Pugh, A. Ransford, A. P. Reed, C. Roman, M. Rowe, C. Ryan-Anderson, S. Sanders, J. Sedlacek, P. Shevchuk, P. Siegfried, T. Skripka, B. Spaun, R. T. Sprenkle, R. P. Stutz, M. Swallows, R. I. Tobey, A. Tran, T. Tran, E. Vogt, C. Volin, J. Walker, A. M. Zolot, and J. M. Pino, A Race-Track Trapped-Ion Quantum Processor, Phys. Rev. X **13**, 041052 (2023).

[10] X.-L. Wang, Y.-H. Luo, H.-L. Huang, M.-C. Chen, Z.-E. Su, C. Liu, C. Chen, W. Li, Y.-Q. Fang, X. Jiang, J. Zhang, L. Li, N.-L. Liu, C.-Y. Lu, and J.-W. Pan, 18-Qubit Entanglement with Six Photons' Three Degrees of Freedom, Phys. Rev. Lett. **120**, 260502 (2018).

[11] C. Song, K. Xu, H. Li, Y.-R. Zhang, X. Zhang, W. Liu, Q. Guo, Z. Wang, W. Ren, J. Hao, H. Feng, H. Fan, D. Zheng, D.-W. Wang, H. Wang, and S.-Y. Zhu, Generation of multicomponent atomic Schrödinger cat states of up to 20 qubits, Science **365**, 574 (2019).

[12] G. J. Mooney, G. A. L. White, C. D. Hill, and L. C. L. Hollenberg, Generation and verification of 27-qubit Greenberger-Horne-Zeilinger states in a superconducting quantum computer, J. Phys. Commun. **5**, 095004 (2021).

[13] C. A. Sackett, D. Kielpinski, B. E. King, C. Langer, V. Meyer, C. J. Myatt, M. Rowe, Q. A. Turchette, W. M. Itano, D. J. Wineland, and C. Monroe, Experimental entanglement of four particles, Nature **404**, 256 (2000).

[14] K. X. Wei, I. Lauer, S. Srinivasan, N. Sundaresan, D. T. McClure, D. Toyli, D. C. McKay, J. M. Gambetta, and S. Sheldon, Verifying multipartite entangled Greenberger-Horne-Zeilinger states via multiple quantum coherences, Phys. Rev. A **101**, 032343 (2020).

[15] J. Baum, M. Munowitz, A. N. Garroway, and A. Pines, Multiple-quantum dynamics in solid state NMR, J. Chem. Phys. **83**, 2015 (1985).

[16] M. Gärttner, J. G. Bohnet, A. Safavi-Naini, M. L. Wall, J. J. Bollinger, and A. M. Rey, Measuring out-of-time-order correlations and multiple quantum spectra in a trapped-ion quantum magnet, Nat. Phys. **13**, 781 (2017).

[17] G. A. Álvarez and D. Suter, NMR Quantum Simulation of Localization Effects Induced by Decoherence, Phys. Rev. Lett. **104**, 230403 (2010).

[18] D. Leibfried, E. Knill, S. Seidelin, J. Britton, R. B. Blakestad, J. Chiaverini, D. B. Hume, W. M. Itano, J. D. Jost, C. Langer, R. Ozeri, R. Reichle, and D. J. Wineland, Creation of a six-atom 'Schrödinger cat' state, Nature **438** (2005).

[19] T. Monz, P. Schindler, J. T. Barreiro, M. Chwalla, D. Nigg, W. A. Coish, M. Harlander, W. Hänsel, M. Hennrich, and R. Blatt, 14-Qubit Entanglement: Creation and Coherence, Phys. Rev. Lett. **106**, 130506 (2011).

[20] C. Song, K. Xu, W. Liu, C.-p. Yang, S.-B. Zheng, H. Deng, Q. Xie, K. Huang, Q. Guo, L. Zhang, P. Zhang, D. Xu, D. Zheng, X. Zhu, H. Wang, Y.-A. Chen, C.-Y. Lu, S. Han, and J.-W. Pan, 10-Qubit Entanglement and Parallel Logic Operations with a Superconducting Circuit, Phys. Rev. Lett. **119**, 180511 (2017).

[21] K. Mølmer, K. Berg-Sørensen, Y. Castin, and J. Dalibard, A monte carlo wave function method in quantum optics, in *J Opt Soc Am* (1992) p. MFF1.

[22] L. Xiang, W. Jiang, Z. Bao, Z. Song, S. Xu, K. Wang, J. Chen, F. Jin, X. Zhu, Z. Zhu, F. Shen, N. Wang, C. Zhang, Y. Wu, Y. Zou, J. Zhong, Z. Cui, A. Zhang, Z. Tan, T. Li, Y. Gao, J. Deng, X. Zhang, H. Dong, P. Zhang, S. Jiang, W. Li, Z. Lu, Z.-Z. Sun, H. Li, Z. Wang, C. Song, Q. Guo, F. Liu, Z.-X. Gong, A. V. Gorshkov, N. Y. Yao, T. Iadecola, F. Machado, H. Wang, and D.-L. Deng, Long-lived topological time-crystalline order on a quantum processor, arXiv:2401.04333 (2024).

[23] M. Developer, Mindquantum, version 0.6.0 (2021).

[24] F. Yan, P. Krantz, Y. Sung, M. Kjaergaard, D. L. Campbell, T. P. Orlando, S. Gustavsson, and W. D. Oliver, Tunable Coupling Scheme for Implementing High-Fidelity Two-Qubit Gates, Phys. Rev. Appl. **10**, 054062 (2018).

[25] B. Foxen, C. Neill, A. Dunsworth, P. Roushan, B. Chiaro, A. Megrant, J. Kelly, Z. Chen, K. Satzinger, R. Barends, F. Arute, K. Arya, R. Babbush, D. Bacon, J. C. Bardin, S. Boixo, D. Buell, B. Burkett, Y. Chen, R. Collins, E. Farhi, A. Fowler, C. Gidney, M. Giustina, R. Graff, M. Harrigan, T. Huang, S. V. Isakov, E. Jeffrey, Z. Jiang, D. Kafri, K. Kechedzhi, P. Klimov, A. Korotkov, F. Kostritsa, D. Landhuis, E. Lucero, J. McClean, M. McEwen, X. Mi, M. Mohseni, J. Y. Mutus, O. Naaman, M. Neeley, M. Niu, A. Petukhov, C. Quintana, N. Rubin, D. Sank, V. Smelyanskiy, A. Vainsencher, T. C. White, Z. Yao, P. Yeh, A. Zalcman, H. Neven, and J. M. Martinis (Google AI Quantum), Demonstrating a Continuous Set of Two-Qubit Gates for Near-Term Quantum Algorithms, Phys. Rev. Lett. **125**, 120504 (2020).

[26] C. Neill, T. McCourt, X. Mi, Z. Jiang, M. Y. Niu, W. Mruczkiewicz, I. Aleiner, F. Arute, K. Arya, J. Atalaya, R. Babbush, J. C. Bardin, R. Barends, A. Bengtsson, A. Bourassa, M. Broughton, B. B. Buckley, D. A. Buell, B. Burkett, N. Bushnell, J. Campero, Z. Chen, B. Chiaro, R. Collins, W. Courtney, S. Demura, A. R. Derk, A. Dunsworth, D. Eppens, C. Erickson, E. Farhi, A. G. Fowler, B. Foxen, C. Gidney, M. Giustina, J. A. Gross, M. P. Harrigan, S. D. Harrington, J. Hilton, A. Ho, S. Hong, T. Huang, W. J. Huggins, S. V. Isakov, M. Jacob-Mitos, E. Jeffrey, C. Jones, D. Kafri, K. Kechedzhi, J. Kelly, S. Kim, P. V. Klimov, A. N. Korotkov, F. Kostritsa, D. Landhuis, P. Laptev, E. Lucero, O. Martin, J. R. McClean, M. McEwen, A. Megrant, K. C. Miao, M. Mohseni, J. Mutus, O. Naaman, M. Neeley, M. Newman, T. E. O'Brien, A. Opremcak, E. Ostby, B. Pató, A. Petukhov, C. Quintana, N. Redd, N. C. Rubin, D. Sank, K. J. Satzinger, V. Shvarts, D. Strain, M. Szalay, M. D. Trevithick, B. Villalonga, T. C. White, Z. Yao, P. Yeh, A. Zalcman, H. Neven, S. Boixo, L. B. Ioffe, P. Roushan, Y. Chen, and V. Smelyanskiy, Accurately computing the electronic properties of a quantum ring, Nature **594**, 508–512 (2021).

[27] X. Mi and *et. al.*, Time-crystalline eigenstate order on a quantum processor, Nature **601**, 531 (2022).

[28] V. Khemani, R. Moessner, and S. L. Sondhi, A Brief History of Time Crystals, arXiv:1910.10745 (2019).

[29] A. Stasiuk and P. Cappellaro, Observation of a Prethermal $U(1)$ Discrete Time Crystal, Phys. Rev. X **13**, 041016 (2023).

[30] A. Kyprianidis, F. Machado, W. Morong, P. Becker, K. S. Collins, D. V. Else, L. Feng, P. W. Hess, C. Nayak, G. Pagano, N. Y. Yao, and C. Monroe, Observation of a prethermal discrete time crystal, Science **372**, 1192 (2021).

[31] B. Huang, Analytical theory of cat scars with discrete time-crystalline dynamics in Floquet systems, Phys. Rev. B **108**, 104309 (2023).

[32] M. Ippoliti, K. Kechedzhi, R. Moessner, S. Sondhi, and V. Khemani, Many-Body Physics in the NISQ Era: Quantum Programming a Discrete Time Crystal, PRX Quantum **2**, 030346 (2021).

[33] X. Mi, M. Sonner, M. Y. Niu, K. W. Lee, B. Foxen, R. Acharya, I. Aleiner, T. I. Andersen, F. Arute, K. Arya, A. Asfaw, J. Atalaya, J. C. Bardin, J. Basso, A. Bengtsson, G. Bortoli, A. Bourassa, L. Brill, M. Broughton, B. B. Buckley, D. A. Buell, B. Burkett, N. Bushnell, Z. Chen, B. Chiaro, R. Collins, P. Conner, W. Courtney, A. L. Crook, D. M. Debroy, S. Demura, A. Dunsworth, D. Eppens, C. Erickson, L. Faoro, E. Farhi, R. Fatemi, L. Flores, E. Forati, A. G. Fowler, W. Giang, C. Gidney, D. Gilboa, M. Giustina, A. G. Dau, J. A. Gross, S. Habegger, M. P. Harrigan, M. Hoffmann, S. Hong, T. Huang, A. Huff, W. J. Huggins, L. B. Ioffe, S. V. Isakov, J. Iveland, E. Jeffrey, Z. Jiang, C. Jones, D. Kafri, K. Kechedzhi, T. Khattar, S. Kim, A. Y. Kitaev, P. V. Klimov, A. R. Klots, A. N. Korotkov, F. Kostritsa, J. M. Kreikebaum, D. Landhuis, P. Laptev, K.-M. Lau, J. Lee, L. Laws, W. Liu, A. Locharla, O. Martin, J. R. McClean, M. McEwen, B. M. Costa, K. C. Miao, M. Mohseni, S. Montazeri, A. Morvan, E. Mount, W. Mruczkiewicz, O. Naaman, M. Neeley, C. Neill, M. Newman, T. E. O'Brien, A. Opremcak, A. Petukhov, R. Potter, C. Quintana, N. C. Rubin, N. Saei, D. Sank, K. Sankaragomathi, K. J. Satzinger, C. Schuster, M. J. Shearn, V. Shvarts, D. Strain, Y. Su, M. Szalay, G. Vidal, B. Villalonga, C. Vollgraff-Heidweiller, T. White, Z. Yao, P. Yeh, J. Yoo, A. Zalcman, Y. Zhang, N. Zhu, H. Neven, D. Bacon, J. Hilton, E. Lucero, R. Babbush, S. Boixo, A. Megrant, Y. Chen, J. Kelly, V. Smelyanskiy, D. A. Abanin, and P. Roushan, Noise-resilient edge modes on a chain of superconducting qubits, Science **378**, 785 (2022).

[34] V. Khemani, C. R. Laumann, and A. Chandran, Signatures of integrability in the dynamics of rydberg-blockaded chains, Phys. Rev. B **99**, 161101 (2019).

[35] M. P. Zaletel, M. Lukin, C. Monroe, C. Nayak, F. Wilczek, and N. Y. Yao, Colloquium: Quantum and classical discrete time crystals, Rev. Mod. Phys. **95**, 031001 (2023).

[36] D. V. Else, B. Bauer, and C. Nayak, Floquet Time Crystals., Phys. Rev. Lett. **117**, 090402 (2016).

[37] N. Y. Yao, A. C. Potter, I.-D. Potirniche, and A. Vishwanath, Discrete Time Crystals: Rigidity, Criticality, and Realizations., Phys. Rev. Lett. **118**, 030401 (2017).

[38] C. W. von Keyserlingk, V. Khemani, and S. L. Sondhi, Absolute stability and spatiotemporal long-range order in Floquet systems, Phys. Rev. B **94**, 085112 (2016).